



1 **Gravity-wave effects on tracer gases and stratospheric**
2 **aerosol concentrations during the 2013 ChArMEx**
3 **campaign**

4
5 **Fabrice Chane Ming¹, Damien Vignelles², Fabrice Jegou², Gwenael Berthet²,**
6 **Jean-Batiste Renard², François Gheusi³ and Yuriy Kuleshov^{4,5}**

7
8 [1] {Université de la Réunion, Laboratoire de l'Atmosphère et des Cyclones, UMR 8105,
9 UMR CNRS-Météo France-Université, La Réunion, France}

10 [2] {CNRS, LPC2E, UMR 7328, CNRS / Université d'Orléans, Orléans, France}

11 [3] {Laboratoire d'Aérodynamique, UMR5560, Université de Toulouse and CNRS, Toulouse,
12 France}

13 [4] {Bureau of Meteorology, Australia}

14 [5] {School of Mathematical and Geospatial Sciences, RMIT University, Australia}

15

16 Correspondence to: F. Chane Ming (fchane@univ-reunion.fr)

17

18

19 **Abstract**

20 Coupled balloon-borne observations of Light Optical Aerosol Counter (LOAC), M10
21 meteorological global positioning system (GPS) sondes, ozonesondes and GPS radio
22 occultation data, are examined to identify gravity-wave (GW) induced fluctuations on tracer
23 gases and on the vertical distribution of stratospheric aerosol concentrations during the 2013
24 ChArMEx (Chemistry-Aerosol Mediterranean Experiment) campaign. Observations reveal
25 signatures of GWs with short vertical wavelengths less than 4 km in dynamical parameters
26 and tracer constituents which are also correlated with the presence of thin layers of strong
27 local enhancements of aerosol concentrations in the upper troposphere and the lower
28 stratosphere. In particular, this is evident from a case study above Ile du Levant (43.02°N,



1 6.46°E) on 26-29 July 2013. Observations show a strong activity of dominant mesoscale
2 inertia GWs with horizontal and vertical wavelengths of 370-510 km and 2-3 km respectively,
3 and periods of 10-13 h propagating southward at altitudes of 13-20 km and eastward above 20
4 km during 27-28 July which is also captured by the European Center for Medium range
5 Weather Forecasting (ECMWF) analyses. Ray-tracing experiments indicate the jet-front
6 system to be the source of observed GWs. Simulated vertical profiles of dynamical
7 parameters with large stratospheric vertical wind maximum oscillations $\pm 40 \text{ mms}^{-1}$ are
8 produced for the dominant mesoscale GW using the simplified linear GW theory. Parcel
9 advection method reveals signatures of GWs in the ozone mixing ratio and the specific
10 humidity. Simulated vertical wind perturbations of the dominant GW and small-scale
11 perturbations of aerosol concentration (aerosol size of 0.2-0.7 μm) are in phase in the lower
12 stratosphere. Present results support the importance of vertical wind perturbations in the GW-
13 aerosol relation. The observed mesoscale GW induces a strong modulation of the amplitude
14 of tracer gases and the stratospheric aerosol background.

15

16

17

18 **1 Introduction**

19 Gravity waves (GWs) affect dynamics of the middle atmosphere for momentum transport and
20 deposition, and mixing above the upper troposphere as well as chemistry and consequently
21 impact on global circulation and climate (Fritts and Alexander, 2003; Geller et al., 2012; Ern
22 et al., 2014). Several previous studies reveal atmospheric waves to be important sources of
23 stratospheric tracer variability. Analytical wave-tracer interaction models help to identify the
24 nature of waves and to quantify amplitudes and effects of waves in the middle atmosphere
25 from observations (Eckermann et al., 1998; Chane Ming et al., 2000; Xu et al., 2000). They
26 are usually used to quantify perturbations induced by GWs on tracer constituents. Small-scale
27 structures were misrepresented by past numerical models and therefore considered as
28 meteorological noise. Thanks to recent progress in computer technologies and improvements
29 in numerical modeling of small-scale structures, most numerical weather prediction models
30 and high-resolution mesoscale numerical models are now capable to produce characteristics
31 of GWs using GW parameterizations or by explicitly resolving convection (Shutts and
32 Vosper, 2011). Nevertheless, comparison between observations and numerical model outputs
33 shows that efforts are still needed to resolve such intermittent small-scale waves (Chane Ming
34 et al., 2014). Thus measuring constituent response using analytical wave-tracer interaction



1 models remains an inexpensive alternative way to derive correct constituent backgrounds and
2 wave related quantities.

3 Aerosols play an important role in meteorology, in radiative processes and in atmospheric
4 chemistry in the free atmosphere (Hobbs, 1993). Stratospheric aerosols are important for a
5 number of processes related to the chemical and radiation balance of the atmosphere and
6 consequently they impact on climate and its variability (Deshler, 2008). Even during
7 volcanically quiescent periods (Hamill et al., 1997; SPARC Report No. 4, 2006) when
8 background stratospheric aerosol loading is low, aerosols may have reduced global warming
9 effects (Solomon et al., 2011). During the process of formation and growth of atmospheric
10 aerosols, the aerosol dynamics and atmospheric chemistry are also coupled with large and
11 small-scale meteorological dynamics. In the troposphere, for example, vertical wind shear can
12 play a dominant role in aerosol-cloud interactions especially in regulating aerosol effects on
13 the strength of isolated deep convective clouds (Fan et al., 2009). In the stratosphere, Hommel
14 et al. (2015) describe how tropical stratospheric aerosol is affected by the quasi-biennial
15 oscillation. Vaughan et al. (1987) report dynamical influences on the short-term variability of
16 stratospheric aerosols from vertical profiles of aerosol backscatter ratio obtained by a high
17 vertical resolution lidar (30 m) and 20 min integration time at Aberystwyth (52.4°N, 4.1°W).
18 Their observations reveal wavelike structures which could be attributed to stratospheric GWs.
19 Tropical waves with periods shorter than a day could also explain some variability in aerosol
20 distribution observed in Indonesia (Matsumura et al., 2001). From a model study, Carslaw et
21 al. (1999) conclude that mountain-induced mesoscale temperature perturbations may be an
22 important source of nitric acid trihydrate particles in the Arctic. Bacmeister et al. (1999)
23 analyze the impact of mesoscale temperature perturbations and heating-cooling rates due to a
24 spectrum of stratospheric GWs on the growth and evaporation of stratospheric nitric acid
25 trihydrate particles. The microphysical trajectory-box model reveals significant scatter in
26 aerosol volume around the thermodynamic equilibrium values as a result of temperature
27 perturbations. Using a Lagrangian-based sectional box model, Nilsson et al. (2000) show that
28 the temperature amplitude of short period waves is the most important wave characteristic
29 controlling the mean nucleation rate and net particle number concentration of 0.5 nm-1µm
30 size classes. They also suggest that GWs could enhance the aerosol nucleation rate up to 5
31 orders of magnitude if the temperature perturbation due to the wave is as strong as 5 K. In
32 addition turbulent mixing and GWs are likely to promote the production of new aerosols
33 (Zahn et al., 2000; SPARC Report N°4, 2006). Thus, previous studies highlight the lack of



1 information on GW-aerosol interactions with measurements, especially to improve aerosol
2 modeling.

3 The present study analyzes GW-induced small-scale variability on high vertical resolution
4 measurements of tracer gases and stratospheric aerosols during the volcanically quiescent
5 period of the 2013 Chemistry-aerosol Mediterranean Experiment (ChArMEx) campaign.
6 Methodology and several complementary analyses based on observations and modeling are
7 described to detect and characterize GWs as well as GW sources. The method is fully
8 illustrated based on a case study on 27 July 2013. Effects of GWs on tracer gases such as
9 ozone and water vapor as well as GW-stratospheric aerosol relation are investigated.

10 The paper is structured as follows. A description of the ChArMEx campaign and the data are
11 presented in Sect. 2 and of methodologies and analyses in Sect. 3. Section 4 describes the
12 synoptic situation on 27 July 2013. Results on the case study on 27 July 2013 are discussed in
13 Sect. 5. Conclusions are drawn in Sect. 6.

14

15

16 **2 Charmex campaign and data description**

17 The ChArMEx campaign (<http://charmex.lsce.ipsl.fr>) is part of the international and regional
18 multidisciplinary initiative Mediterranean Integrated STudies at Regional And Local Scales
19 (MISTRALS). It aims at improving the characterization of short-lived (≤ 1 month) particulate
20 and gaseous tropospheric trace species responsible for atmospheric pollution over the
21 Mediterranean Basin, and evaluating its impacts on the present and future state of the
22 atmospheric environment. The campaign occurred during the Northern Hemisphere summer
23 from 10 June to 10 August 2013. In addition to ground-based observations, airborne
24 operations were organized during two special observation periods (SOPs). The first SOP from
25 12 June to 5 July was dedicated primarily to the study of interactions between aerosols and
26 radiation balance and the second one from 23 July to 9 August to the study of chemical
27 processes and more particularly to the formation of secondary aerosols.

28 Light Optical Aerosol Counter (LOAC) is a light and compact optical counter which has been
29 designed to perform measurements of aerosols from the ground to the middle stratosphere (up
30 to 37 km heights) carried by all types of balloons in various atmospheric conditions (Renard
31 et al., 2015). During balloon ascent, it provides information on the concentration and size
32 distribution of aerosols on 19 size classes from 0.2 μm to $\sim 50 \mu\text{m}$ in diameter every ten



1 seconds (≈ 50 -m heights), as well as the main nature of particles (carbonaceous aerosol,
2 mineral, droplets of water or sulfuric acid). The technique is based on the observation of the
3 scattered light by particles at two angles (Lurton et al., 2014). The instrument can count up to
4 ~ 3000 particles smaller than $1 \mu\text{m}$, about $20 \text{ particles cm}^{-3}$ for particles larger than $1 \mu\text{m}$ in
5 dry conditions and up to $200 \text{ particles cm}^{-3}$ in fog/cloud conditions. For the LOAC integration
6 time of 10 s, the counting uncertainty at 1-sigma is about $\pm 15 \%$ for concentrations greater
7 than $10^{-1} \text{ particles cm}^{-3}$. Renard et al. (2015a, b) provide a detailed description of the
8 instrument as well as information on calibration and validation of measurements with cross-
9 comparisons with different instruments during several campaigns.

10 Electrochemical concentration cell (ECC) ozonesondes developed by Komhyr (1969) are the
11 most commonly used worldwide for tropospheric and stratospheric ozone soundings (Smit et
12 al., 2007; GAW, 2011). The measurement principle is based on the electric current of a few
13 μA generated through the cell as consequence of oxidation of iodide ions by ozone contained
14 in ambient air bubbling in a potassium iodide electrochemical solution. The typical response
15 time to an ozone concentration step change is 20-30 s, so that the practical vertical resolution
16 for a balloon ascending at 5 ms^{-1} is around 100-150 m, even though ozone data are provided
17 every second. The ozone measurement accuracy is within 5% in the stratosphere but is worse
18 in the troposphere, around 10%, owing to lower ambient ozone concentrations.

19 Nineteen LOAC sondes and fifteen ECC ozonesondes were launched using meteorological
20 balloons during ChArMEx in summer 2013, from Minorca Island (39.99°N , 4.25°E) in Spain
21 during SOP1 and from Ile du Levant (43.02°N , 6.46°E) in France during SOP2. Both LOAC
22 aerosol and ECC ozone sensors were integrated with Meteo Modem Company global
23 positioning system (GPS) M10 radiosondes (RSs). Temperature, horizontal wind speed and
24 direction are sampled every 1 s (≈ 5 -m heights) and have resolution of 0.1 K, 0.15 ms^{-1} and
25 0.1° respectively. The capacitor-type humidity sensor of M10 GPS sondes produces humidity
26 measurements with resolution and total instrumental error of 1% and $\pm 5\%$ respectively.

27 Radio occultation measurements (GPS-RO) are obtained from CDAAC (COSMIC Data
28 Analysis and Archive Center). About 120 vertical wet temperature profiles at altitudes from 2
29 to 40 km at longitudes of 20°W - 10°E and latitudes of 30° - 55°N are available between 26 and
30 29 July 2013. Measurements have high accuracy for temperature $< 1 \text{ K}$ at heights between 5
31 km and 25 km and vertical resolution varying from about 0.5 km in the lower stratosphere
32 (LS) to 1.4 km at 40 km heights in the middle atmosphere (Kursinski et al., 1997). For a lower
33 limit of 1.4-km vertical wavelength (λ_v) in the upper troposphere and the lower stratosphere



1 (UTLS), the corresponding horizontal line-of-sight resolution, i.e., the lower limit of
2 horizontal wavelength (λ_h) of an observed GW is about 270 km (Kursinski et al. 1997;
3 Hindley et al., 2015). If the horizontal line-of-sight and the horizontal wave vector are not
4 aligned, GWs with shorter horizontal wavelength can be captured. Depending on the influence
5 of the geometric wave parameters and the measurement geometry on a homogeneous
6 spectrum of GWs in the range 100-1000 km horizontal and 1-10 km vertical wavelengths,
7 more than 80% of GW total variance of the spectrum can be derived (Lange and Jacobi,
8 2003). Previous climatological studies of GWs in the stratosphere have been derived from
9 GPS Radio Occultation (RO) data (Tsuda et al., 2000, Liou et al., 2006). In particular, Chane
10 Ming et al. (2014) used RO data to complement RS observations and modeling for the
11 characterization of mesoscale GWs produced by a tropical meteorological event: the tropical
12 cyclone *Ivan* over the south-west Indian Ocean.

13

14 **3 Methodology and analyses**

15 **3.1 Pre-processing and noise-reduction**

16 Vertical profiles of temperature, horizontal wind speed and ozone concentration are first re-
17 sampled with a 5-m vertical resolution applying a cubic spline interpolation. Profiles of
18 LOAC aerosol concentration are interpolated at every 50-m using a nearest neighbor
19 interpolation. Then, vertical profiles are filtered using a discrete wavelet transform
20 (DWT) also called multiresolution analysis. Multiresolution is well adapted for the analysis
21 and the decomposition of multiscale wavelike structures in geophysical signals (Kumar, 1997,
22 Domingues et al., 2005). Conventional filters often alter amplitudes and/or phase of the
23 original signal when filtering out high-frequency structures. Implementing finite impulse
24 response filters with properties such as perfect flatness in the passband, very fast decay at the
25 frequency cutoff and linear phase response is difficult and expensive. In the present study, the
26 wavelet decomposition consists of the fast application of an orthogonal filter bank, i.e., a set
27 of iterated so that the remaining signal (the approximation) becomes coarser and coarser after
28 each iteration. Then the signal can be perfectly reconstructed by adding all details and the
29 approximation of the signal at the n^{th} order of the iteration (refer to equation 1 in Chane Ming
30 et al., 2000a). The smoothness or the number of vanishing moments of the wavelet are
31 important in theoretical and practical studies (Pollicot and Weiss, 2008) because it ensures
32 fast decay and limits the wavelet to capture high order polynomial behavior in a noisy signal.



1 But more wavelet values are needed to capture most of the energy of the signal when the
2 smoothness of the wavelet increases, i.e., the support of the wavelet is less compact (Walker,
3 2008). Compact support orthogonal bases with high orders of smoothness such as the eighth-
4 order Daubechies wavelet ensures energy conservation and a very good localization both in
5 space and frequency for the analysis of GWs in the lower and middle atmosphere.
6 Applications of the pyramid algorithm and the eighth-order Daubechies wavelet coefficients
7 are described in Chane Ming et al. (1999, 2000a). In this way, fine structures with $\lambda_v < 0.32$
8 km are efficiently removed from re-sampled profiles.

9 Perturbation profiles are then extracted from filtered data using a numerical Butterworth
10 infinite impulse response high-pass filter with a specific vertical wavelength cutoff between
11 5-7 km for temperature, horizontal wind, and ozone concentrations. Mean profiles result from
12 the difference between the original and perturbation profiles. A high-order Butterworth filter
13 is commonly used to simulate an ideal filter with maximally-flat and linear phase responses in
14 the pass-band. A fourth-order Butterworth filter provides a good compromise between the
15 cost of implementation and the frequency decay (-80 dB/decade). Because of the high
16 variability of aerosol concentration with altitude, the DWT is used to extract perturbations of
17 aerosol concentration with a vertical wavelength cutoff of 6.4 km.

18 Figure 1 shows examples of 50-m interpolated continuous vertical distributions of aerosol
19 concentrations with diameters of 0.2-50 μm in the troposphere and the stratosphere up to the
20 altitude of 35 km (Fig. 1b). Different shapes of vertical distribution are observed. In
21 particular, Figure 1c visualizes a stratospheric aerosol layer with high values of aerosol
22 concentration in which thin layers of strong local enhancements are embedded. Severe storms
23 with numerous lightning strikes occurred in France for cases in Figures 1a, 1c and 1d. The
24 examination of the whole aerosol dataset indicates a day to day variability of aerosols in the
25 UTLS. Other cases reveal that aerosol content was low in the UTLS during ChArMEx.

26

27 **3.2 Detection of GW structures**

28 Cases for which aerosol layers are visualized in the UTLS are analyzed by the continuous
29 wavelet transform (CWT) to detect GW signatures (Chane Ming et al., 2000a). The
30 continuous wavelet transform with Morlet complex-valued mother wavelet is applied to
31 perturbation profiles of temperature, horizontal wind speed, ozone and concentration of
32 aerosols to produce altitude-wavelength representations of the modulus of CWT coefficients,



1 also called scalograms. For vertical profiles in Figure 1, scalograms capture similar signatures
2 of wavelike structures with vertical wavelengths between 1 and 4 km in dynamical parameters
3 and tracer constituents of ozone and aerosols in the UTLS which are explained by the
4 presence of GWs. The case on 27 June 2013 is described in section 4.

5 The European Center for Medium range Weather Forecasting (ECMWF) model is an
6 operational numerical weather prediction model which can explicitly resolve stratospheric
7 GWs with horizontal and vertical wavelengths > 200 km and > 2 km respectively (Shutts and
8 Vosper, 2011; Preusse et al., 2014; Chane Ming et al., 2014). Distributions of vertical velocity
9 and horizontal wind divergence produce snapshots of GW structures. A 1-D fast Fourier
10 transform (FFT) in latitude is applied on 6-hourly ECMWF operational analyses with $1.125^\circ \times$
11 1.125° resolution at 50 hPa (about 21 km) in the LS to produce spectral densities of dominant
12 GWs as a function of latitudes and horizontal wavelengths.

13

14 **3.3 Characterization of GWs**

15 Conventional methods detailed in Chane Ming et al. (2010) such as the hodograph analysis,
16 the SPARC Gravity Wave Initiative Radiosonde Data and Stokes' parameter methods
17 (Eckermann, 1996; Vincent et al., 1997) are applied to RS vertical perturbation profiles to
18 provide characteristics of GWs (energy densities, momentum fluxes and spectral parameters).
19 The hodograph analysis computes the intrinsic frequency from the elliptical axis ratio which
20 is determined from variances of horizontal wind perturbations as a function of altitude.
21 Combined conventional methods (CCM) based on the SPARC and Stokes' parameter
22 methods ensure good estimation of GW spectral characteristics. The wavenumber, the
23 direction of horizontal propagation and the phase speed of horizontal propagation are derived
24 from the SPARC method and the intrinsic frequency is obtained from the Stokes' parameter
25 method.

26 The phase shift divided by the distance between two adjacent vertical profiles of temperature
27 in space and time at a given altitude provides the horizontal wavenumber projected along the
28 line connecting the two profiles. Ern et al. (2004) introduced this method to estimate global
29 absolute values of vertical flux of horizontal momentum from CRISTA data for horizontal and
30 vertical wavelengths > 400 km and > 5 km respectively. The method is adapted to pairs and
31 triads of RO temperature profiles using the S-transform and CWT to estimate the phase shift
32 of horizontal wavelengths for horizontal and vertical wavelengths > 1500 km and > 5 km



1 (Wang and Alexander, 2010; Faber et al., 2013). In the present study, RS and RO temperature
2 profiles are combined to analyze GWs with shorter horizontal and vertical wavelengths than
3 those described in previous studies.

4

5 **3.4 Simulated GWs**

6 The GW parameters are used to initialize a model based on the simplified linear wave
7 polarization relations for vertically propagating internal waves in a rotating fluid (Gill, 1982;
8 Chane Ming et al., 2002) to produce synthetic vertical profiles of temperature and horizontal
9 winds with GW signatures. Input parameters are vertical wavelength, intrinsic frequency,
10 direction of horizontal propagation, localization, altitude range, amplitude of temperature
11 perturbation and mean profiles of temperature and horizontal winds. A Gaussian-shaped
12 sinusoidal pulse is first computed at the observed altitude range from temperature
13 perturbations. Based on the simplified linear wave polarization relations, vertical wind
14 perturbations are derived from temperature perturbations. Then the horizontal wind
15 perturbations result from the vertical wind perturbations when the rotated frame of reference
16 is aligned along the horizontal wavenumber. The direction of horizontal wave propagation is
17 finally used to rotate the frame of reference to obtain observed horizontal wind perturbations.
18 The simulated profiles result from the sum of perturbations and observed background profiles.

19

20 **3.5 Ray-tracing**

21 The Gravity Wave Regional or Global Ray Tracer (GROGRAT) is a four-dimensional ray-
22 tracing model of the propagation and amplitude evolution of non-hydrostatic GWs in rotating,
23 stratified, compressible slowly-varying background described by numerically gridded fields
24 of temperature, wind and pressure or geopotential height in the lower and middle atmosphere.
25 It is based on the dispersion and refraction of the ray paths and includes parameterizations of
26 turbulent and radiative wave damping and of wave-amplitude saturation. A full description of
27 the model can be found in Marks and Eckermann (1995) and Eckermann and Marks (1997).
28 The ray path stops when the vertical wavelength becomes too large or varies too quickly with
29 altitude, in particular near GW sources. Previous studies have shown that GROGRAT is an
30 efficient tool to identify GW sources (Guest et al., 2000, 2002) and to simulate GW-
31 background interactions such as GW effects, wave filtering, space and time variability of GW
32 activity and characteristics. For example, GROGRAT simulations help to interpret global GW



1 observed morphology derived from satellite observations (Preusse et al., 2009). In the present
2 study, the model GROGRAT is run with observed GW spectral characteristics in a regional
3 background of 6-hourly operational ECMWF analyses of temperature, horizontal wind and
4 geopotential height with resolutions of 25 pressure levels (1000-1 hPa) and $1.125^\circ \times 1.125^\circ$
5 in the horizontal plane.

6

7 **3.6 Parcel advection method**

8 The parcel advection method is based on an analytical formula for the linear response of
9 minor constituents to non-dissipating hydrostatic internal GW motions when photochemical
10 response of the constituent can be negligible, especially for long lived tracers. The method
11 was used for GW-induced perturbations in ozone, water vapor and other constituents such as
12 nitrogen dioxide and sodium (Randel, 1990; Teitelbaum et al., 1994).
13 When the photochemical response of the constituent is negligible, in the linear simplified
14 case, normalized ozone mixing ratio perturbations as a function of altitude are linked to
15 normalized potential temperature perturbations by a coefficient $R(z)$ which is the ratio of
16 vertical gradients of ozone and of the potential temperature background. Chane Ming et al.
17 (2000b) illustrated the method to produce a climatology of laminae with vertical wavelengths
18 < 5 km induced by GWs and horizontal advection in the UTLS near the southern subtropical
19 barrier. The method also revealed the presence of GWs on vertical ozone profiles collected at
20 Macquarie Island (54°S , 159°E) during the Airborne Southern Hemisphere Ozone
21 Experiment/Measurements for Assessing the Effects of Stratospheric Aircraft
22 (ASHOE/MAESA) observation programme in 1994 (Chane Ming et al., 2003). Eckermann et
23 al. (1998) formalized the method to derive analytical formulas for the response of vertical
24 constituent profiles of arbitrary shape to adiabatic GWs. In particular, they showed that the
25 parcel method becomes inaccurate for non-hydrostatic GWs and if the wave-induced
26 photochemical response produces a significant diabatic feedback on the GW for shorter-lived
27 constituents.

28

29 **4 Synoptic situation on 27 July 2013**

30 A heat wave accompanied by local severe thunderstorms affected the whole of France during
31 July 2013, especially during the second part of the month from 15 to 28 July with local
32 maximum temperatures $> 35^\circ\text{C}$ on 25-27 July. Météo-France ranked it the third hottest July



1 since 1900. As for thunderstorm activity, a total of 527,496 lightning strikes were registered.
2 The most severe stormy episode of the year occurred on 27 July 2013 when both synoptic
3 observations and forecasts indicated the presence of a meteorological pattern similar to an
4 upper level jet streak. A jet streak is characterized by localized wind maxima along the axis of
5 a jet stream and often referred as a jet-front system because it is generally found in association
6 with frontal zones in the UT (Cunningham and Keyser, 2003). Right entrance and left exit
7 regions of jet streaks (with right and left set by the axis of the jet core and defined facing
8 downstream) are preferred areas of storm development characterized by front systems (Lin,
9 2007). Thus, such feature plays a role in the development of mesoscale convective complexes.
10 Climatologies at latitudes of North America reveal that jet streaks are intrinsically linked to
11 tornado and severe storm reports (Rose et al., 2004; Clarke et al., 2009). From a
12 climatological survey of such synoptic patterns, Uccellini and Koch (1987) show the
13 existence of mesoscale GW disturbances which can severely impact on the weather
14 conditions. For operational forecasting and detection of such GWs, Koch and O'Handley
15 (1997) propose a conceptual model with location of GW occurrence in a diffluent region
16 bounded by the 300-hPa ridge axis to the northeast and the 300-hPa inflection axis to the
17 south-west. The southern boundary of the wave region is defined by the location of a surface
18 warm front. Numerical mesoscale studies also support exit regions of jet-front systems at the
19 cold side of surface front as a favorable area of GW generation (O'Sullivan and Dunkerton,
20 1995; Zhang, 2004). Recently Plougonven and Zhang (2014) presented a review of current
21 knowledge and understanding of GWs near jets and fronts from observations, theory, and
22 modeling including jet streaks.

23 On 27 July 2013, mean wind speed was about 150 kmh^{-1} near the tropopause above the
24 western part of France. A sequence of 15-min georeferenced infrared GMS-3 satellite images
25 reveals increasing convective activity associated with the jet-front system on 27 July from
26 0300 UTC. Very warm, moist and unstable air coming from the south triggered a strong
27 mesoscale storm like a bow structure along the north-west coast of France propagating north-
28 eastward in the afternoon of 27 July.

29 Figure 2a depicts the meteorological situation on 27 July at 1200 UTC derived from
30 operational ECMWF analyses, which represents a typical jet streak (refer to Figure 2 in Koch
31 and Hadley (1997)). Isohypses on a 500-hPa meteorological chart visualize the synoptic
32 pattern with a strong minimum of geopotential heights located at 45°N of latitude and 15°W
33 of longitude which strengthens the jet wind field. Maximum wind speed ($>50 \text{ ms}^{-1}$ from 1200



1 UTC) at 300 hPa located west of Portugal indicates the presence of a significant jet streak.
2 Height-longitude cross-section of potential vorticity at 43°N (not shown) shows the presence
3 of a tropopause fold (6°W) located west of the jet (4°W). This observation is supported by the
4 cross-section of ozone mass mixing ratio visualizing a stratospheric intrusion of ozone in the
5 middle troposphere at longitudes between 6°W and 2°W. Turbulent mixing processes within
6 the tropopause fold are first-order importance as a mechanism for stratospheric-tropospheric
7 exchange (Shapiro, 1980). The jet streak dissipated on the afternoon of 28 July.

8 Backward air mass trajectories are calculated with the FLEXible TRAjectories (FLEXTRA)
9 5.0 code, a kinetic trajectory calculation code (Stohl et al., 1995, 2005). Trajectories were
10 initialized with global 3-hourly ECMWF wind fields with 1°x1° horizontal resolution during
11 10 days from 27 July at 2300 UTC at every 1-km height between 15 km to 25 km above Ile
12 du Levant (Fig. 2b). Trajectories reveal two different eastern air masses in the LS originated
13 from tropical UT and mid-latitude LS. The vertical profile of aerosol concentration at Ile du
14 Levant shows evidence of two layers of large amount of aerosols with diameters between 0.2
15 and 50 µm at altitudes of 15-20 and 20-25 km heights and a minimum at 20 km heights where
16 the zonal wind reverses (Fig. 3). During volcanically quiescent period, previous studies
17 mention the presence of a stratospheric sulfate aerosol layer also called the Junge layer with a
18 quasi-steady state relative maximum in particle number concentration ($r > 0.1\mu\text{m}$) around 20
19 km in the mid-latitudes (Junge et al., 1961). Recent observations also reveal the presence of
20 carbonaceous material in stratospheric aerosol (Murphy et al., 2007). In the present study, the
21 "speciation index" retrieved from the 12 and 60° channels LOAC measurements suggests that
22 the nature of stratospheric aerosols with diameters $< 1\mu\text{m}$ is mainly carbonaceous in the LS
23 on 27 July above Ile du Levant (Renard et al., 2015a). Low aerosol content is observed in the
24 LOAC profile of aerosol concentration on 28 July at 1524 UTC when the jet streak dissipates
25 after 1200 UTC. Thus, dynamical processes might be involved in shaping the local
26 stratospheric aerosol background.

27

28 **5 Results**

29 The methodology and the analyses described in section 3 are now illustrated on the case study
30 of 27 July 2013.

31

32 **5.1 Detection of GWs**



1 Figure 3 visualizes filtered resampled vertical profiles of temperature, potential temperature,
2 horizontal winds and ozone from radiosondes and the vertical profile of LOAC aerosol
3 concentrations with diameters of 0.2-0.7 μm on 27 July at 2303 UTC above Ile du Levant.

4 In our study, GW analyses are applied on the sum over the size classes between 0.2 and 0.7
5 μm of continuous vertical profiles of aerosol concentrations to derive a mean continuous
6 vertical profile of aerosol concentrations. Because of the synoptic meteorological event, a
7 sheared tropospheric jet is observed at 10-km heights with maximum wind velocities $<20 \text{ ms}^{-1}$
8 at altitudes of 6 km and 14 km while larger amplitudes ($\approx 40 \text{ ms}^{-1}$) are observed at longitudes
9 $<2.5^\circ\text{W}$ at heights of about 12.5 km. Perturbation profiles are obtained from subtraction
10 between original and background profiles (Chane Ming et al., 2010). They show evidence of
11 wavelike structures with short vertical wavelengths of 2-3 km in temperature and horizontal
12 wind at heights of 13-20 km. Maximum temperature and wind perturbations are about 3°C
13 and $5\text{-}7.6 \text{ ms}^{-1}$ respectively near the tropopause located at the height of 15-km. Large variation
14 in ozone and aerosol perturbations are also observed at altitudes of 15-20 km. Thus the CWT
15 is applied on vertical profiles of perturbations to localize wavelike structures in altitude-
16 wavelength representations at heights below 23 km (refer to section 3.2). The scalograms of
17 the dynamical variables (temperature, wind) reveal a spectral signature with 2.6-km vertical
18 wavelength at heights 10-20 km (Fig. 4a, b, c). For ozone and aerosols, similar peaks are
19 found above 15 km (Fig. 4d, e). Such pattern is also observed on CWTs of each vertical
20 aerosol concentration profile of the five smallest size classes. Analyzing normalized ozone
21 perturbation profiles enhances ozone peak at 13 km heights because of low level tropospheric
22 ozone background whereas the use of ozone perturbation profiles focuses on wavelike
23 structures observed at 15-23 km heights. The cross-sections of potential vorticity and ozone
24 mixing ratio at 43°N indicate that the peak at 13 km heights results from a local stratospheric
25 intrusion at longitudes of $7\text{-}12^\circ\text{W}$. The longitude-latitude maps at 250-300 hPa support the
26 presence of a filament structure of potential vorticity and ozone mass mixing ratio during the
27 jet-streak event (not shown). These observations also suggest that aerosols observed on the
28 LOAC profile at the same altitude are of stratospheric origin on 27 July at 1200 UTC (Plumb
29 et al., 1994).

30 The Morlet CWT local maxima also called “skeleton” (Chane Ming et al., 2000a) provide a
31 continuous distribution of the dominant wavelike structure with the vertical wavelength of 2-3
32 km at heights between 3 km and 25 km with maxima at heights of 13-18 km in zonal wind
33 perturbations (not shown). The vertical wavelength is estimated at about 2.5 km at altitudes of



1 3-7 km. The amplitudes as well as the vertical wavelength decrease rapidly
2 at altitudes above 20 km likely because waves are both filtered at the critical level where
3 intensity of zonal wind approaches zero. The FFT also supports the presence of a dominant
4 wavelike structure with vertical wavelengths of 2-3.5 km at heights of 13-23 km in all
5 analyzed parameters (Fig.4f).

6 The DWT decomposition reveals that RS horizontal wind components (u and v) with
7 dominant vertical wavelengths of 2-3 km are in quadrature at heights of 14-26 km in
8 agreement with the linear GW polarization relation. The hodograph of wind perturbations
9 visualizes elliptical structures with characteristics of GWs with vertical wavelength of about 2
10 km at heights of 14-24 km. The sign change at heights of 9-12 km with anticyclonic
11 (cyclonic) rotation of the ellipse above 12 km (below 9 km) indicates an upward (downward)
12 flux of GW energy. This suggests that GW sources are localized at heights between 9 and 12
13 km.

14 The analyses of vertical velocities in pressure coordinates ($\omega=dp/dt$) derived from ECMWF
15 operational analyses indicate that the numerical weather prediction model captures wavelike
16 structures on 27 July 2013 at 1800 UTC in the LS (Fig. 5). Figure 5a depicts a mesoscale
17 structure located over the eastern part of France. Spectral density of vertical velocities is
18 calculated for longitudes of 10°W-20°E at every latitude step. In particular, the energy of
19 mesoscale wavelike structures with horizontal wavelength in the east-west direction $\lambda_x < 500$
20 km is well-localized at the latitude of 46 °N which corresponds to the latitude of the exit
21 region of the jet streak between latitudes of 42° and 52°N (Fig. 5b). The figure also suggests
22 the presence of longer horizontal structures ($500 \text{ km} < \lambda_x < 2000 \text{ km}$) at latitudes of 45-52°N.
23 But estimated horizontal wavelengths might be biased at latitudes outside the interval 42° and
24 47° where the observed mesoscale structures could not be considered
25 to be plane waves with north-south oriented wave fronts. Figure 5c displays the energy
26 distribution of dominant wavelike structures at latitudes of 42-52°N for horizontal
27 wavelengths $\lambda_x < 1500 \text{ km}$. In particular, it highlights modes with horizontal wavelengths λ_x
28 of 400-800 km with a dominant mode of 400 km at latitudes of about 46°N. The spectral
29 densities at latitudes of 42-48°N and 46°N confirm that the mode of 400 km is dominant at
30 46°N within the wavelength range of 400-800 km (Fig. 5d). The vertical velocity data also
31 reveals that the structure with amplitudes $< 0.2 \text{ Pas}^{-1}$ extends at longitudes (latitudes) between
32 4°W to 10°E (42°N to 52°N).



1 The RO data from 26 July to 29 July 2013 are examined to study the energy activity of
2 wavelike structures with vertical wavelengths of 1.5-5 km (Fig. 6a). The RO soundings over
3 France are mostly located at longitudes of 2.5°-6°E and latitudes of 40-50°N where wavelike
4 structures are well observed in the ECMWF analyses. The spectral analyses of RO
5 temperature profiles support the presence of a strong energy activity of wavelike structures
6 ($\lambda_v < 5$ km) in the area. Figure 6b indicates that spectral density peaks for dominant modes
7 with vertical wavelengths of 2-3.5 km, especially from 27 July at 0600 UTC to 29 July in the
8 morning with a maximum observed on 28 July early in the morning.

9 Thus both observations and ECMWF analyses suggest that the strong activity of GWs with
10 vertical and horizontal wavelengths of 2-5 km and < 1700 km with a dominant mesoscale
11 structure of 400-km horizontal wavelength is associated with the jet-front system from 27 July
12 afternoon to 28 July in the morning in the eastern part of France (refer to the following section
13 5.2).

14

15 **5.2 Spectral characteristics of GWs**

16 The hodograph analysis and the CCM (refer to section 3.3) are applied on RS temperature and
17 wind perturbations on 27 July at 2303 UTC above Ile du Levant to compute spectral
18 characteristics such as vertical and horizontal wavelengths, intrinsic frequencies, periods,
19 directions of horizontal wave propagation and wave energy densities (Table 1). Consistent
20 spectral parameters are obtained, in particular the two methods detect a mesoscale inertia GW
21 with vertical and horizontal wavelengths of 2.6 km and 440-510 km respectively, a period of
22 about 12 h, propagating southward at heights of 13-20 km. Eastward dominant modes with
23 similar vertical wavelength, a period of about 15 h and longer horizontal wavelengths (≈ 1300
24 km) are observed at heights of 20-26 km. The horizontal phase speed of the mesoscale GW is
25 estimated at about 6.8 ms^{-1} (7.9 ms^{-1}) at heights of 13-20 km (20-26 km). GWs with 1300-km
26 horizontal wavelength have larger phase speed of about 24 ms^{-1} at heights of 20-26 km.
27 Consistent large values of total energy densities of about 16 J.kg^{-1} and vertical flux of
28 horizontal momentum of $0.05 \text{ m}^2\text{s}^{-2}$ (vertical flux of zonal momentum $\overline{u'w'} \approx 0.045 \text{ m}^2\text{s}^{-2}$)
29 defined in Vincent et al., (1997) are calculated at heights of 13-20 km. In particular the kinetic
30 energy densities are about three times as large as potential energy densities (spectral
31 index ≈ 2.6 -2.9) which means an excess of wave energy near the inertial frequency (Vincent et
32 al., 1997; Hertzog et al., 2002). A large decrease of total energy densities above heights of 20



1 km indicates that most tropospheric GWs are not transmitted to higher stratospheric layers.
2 The wave energy propagates upward from the troposphere with a fraction of upward energy
3 $F_{up} > 86\%$ (95%) at heights of 13-20 km (20-26 km). In addition the hodograph analysis
4 reveals the presence of a mesoscale structure propagating south-westward with vertical and
5 horizontal wavelengths of 2.6 km and 161-451 km respectively with periods of 10-15h at
6 heights of 3-7 km in the lower troposphere. The F_{up} value of about 60% suggests that wave
7 energy equally propagates upward and downward below the dominant GW tropospheric
8 source. Finally, conventional methods provide good estimates of spectral GW parameters
9 as can be seen from consistent values of the two methods and the standard deviation
10 computed for the hodograph analysis. Similar results are also obtained by the CWT method
11 described in Chané Ming et al. (2002, 2003).

12 The horizontal wavelength is estimated from a triad of temperature profiles from RS at 2303
13 UTC (hereafter called RS2723) on 27 July above Ile du Levant and RO at 0200 UTC
14 (hereafter called RO2802) and 1200 UTC (hereafter called RO2812) on 28 July (Fig. 7a). Here,
15 a high-resolution RS profile is used as a reference for identifying wavelike structures with
16 vertical wavelengths of 2-4 km in RO data. The vertical profiles of temperature perturbation
17 visualize GW signatures at heights of 10-20 km. Phase shifts (Φ) between perturbation
18 profiles are directly calculated for each pair of profiles at heights of 15-20 km where a
19 dominant wavelike structure is detected in the RS profiles (refer to Table 1). Horizontal
20 wavelengths are estimated at about 430 km ($\Phi=2.65$ radians, distance=179.14 km), 551 km
21 ($\Phi=5.24$ radians, distance=459.53 km) and 560 km ($\Phi=3.14$ radians, distance=280.4 km)
22 from the three pairs of vertical profiles respectively (RS2723 and RO2802, RS2723 and
23 RO2812, RO2802 and RO2812). The minimum value of 430 km is the nearest estimation of
24 the real value of the horizontal wavelength (Faber et al., 2013). The phase shift is also
25 computed using the CWT of temperature perturbations. Both figures 7b and 7c show evidence
26 of a similar dominant mode at heights of 10-18 km with vertical wavelengths of 2.5-3 km as
27 the cross-wavelet spectrum depicted on Figure 7d. Phase shift is derived from the cross-
28 wavelet spectrum for the observed dominant mode with vertical wavelengths of 2.5-3.5 km
29 and converted to horizontal wavelength. The second panel of Figure 7d shows evolution of
30 the estimated horizontal wavelength as a function of altitude for vertical wavelengths of 2.5-3
31 km. The horizontal wavelengths vary between 400 km and 680 km at heights of 10-20 km. An
32 additional phase error may be introduced between GPS RO and the radiosonde/GPS RO pairs
33 due to radiative transfer and retrieval (Preusse et al., 2002). Using Eq. 7 reported in Ern et al.



1 (2004), the vertical flux of momentum is estimated at $0.03 \text{ m}^2\text{s}^{-2}$ at heights of 10-20 km. It
2 underestimates the vertical flux of momentum of $0.05 \text{ m}^2\text{s}^{-2}$ previously computed for this
3 case. Characteristics of GWs are consistent with previous observations of inertia GWs
4 associated with a jet stream exit region (Thomas et al., 1999; Ravetta et al., 1999; Bertinet al.,
5 2001). The observed characteristics are used in the next section to provide a linear model of
6 the mesoscale GW and to identify its source.

7

8 **5.3 Simulated profiles and ray-tracing**

9 The spectral parameters (a vertical wavelength of 2.6 km, a period of 11.7 h, a direction of
10 horizontal wave propagation clockwise from north of 204°) at heights of 12.8 km with a
11 height range of 14 km are used to produce synthetic RS profiles with the signature of such a
12 dominant mesoscale GW with upward propagation of energy (refer to section 3.4). Because of
13 the variation of the Brunt-Väisälä frequency with height, the horizontal wavelength, computed
14 using the GW dispersion relation, has values of $225.3 \pm 22.6 \text{ km}$ and $499.9 \pm 45.7 \text{ km}$ at
15 heights of 3-7 km and 13-20 km respectively. A value of $392.7 \pm 13.6 \text{ km}$ is estimated at
16 heights of 13 km. Filtered and simulated amplitudes, and phase relations of perturbations are
17 in good agreement (Fig.8). The hodograph analysis and the CCM are applied on simulated
18 profiles to retrieve spectral parameters (Table 1). The two methods provide good estimates of
19 the original spectral parameters as well as energy densities at heights of 13-20 km. The wave
20 energy propagates upward from the troposphere with a fraction of upward energy $F_{up} > 93 \%$
21 and a horizontal phase speed of 6.44 ms^{-1} at heights of 13-20 km. In particular the structure
22 has a horizontal wavelength of about 200 km in the lower troposphere. In conclusion, results
23 indicate that the mesoscale inertia GW structure agrees well with simplified linear GW theory
24 and that it is the most dominant structure observed in the RS profiles on 27 July. Because of
25 the shape of the wavelike structure, the Morlet complex-valued mother wavelet reveals to be
26 well-adapted to analyze such a structure.

27 Taking into account uncertainties of spectral parameters (Table 1) obtained by the two
28 methods, spectral characteristics of the mesoscale inertia GW with horizontal wavelengths of
29 300-550 km (step of 20 km), ω/f of 1.4-1.8 (step of 0.1) and horizontal propagation direction
30 of 200° at heights of 19 km from 28 July at 0000 UTC are used to define a discrete spectrum
31 of 65 individual components to initialize the GROGRAT model (refer to section 3.5).
32 Backward ray trajectories are computed with the same parameterizations used in Guest et al.



1 (2000) and a time step of 6 min. Almost all rays can be traced back until 12 h-17 h before
2 release on 28 July at 0000 UTC. Projected ray paths on the georeferenced infrared GMS-3
3 image at 1200 UTC and the latitude-height cross section of zonal wind at longitude 0° at 1200
4 UTC reveal that ray paths terminate at the location of the cold frontal zone and at about
5 heights of 10 km in the jet core on 27 July at 1200 UTC at longitudes of 2°-0°W and latitudes
6 of 42.5°-45°N (Fig. 9a, 9b). Figure 9c shows the evolution of the mean horizontal wavelength
7 and the normalized intrinsic frequency as a function of altitude and mean time. The horizontal
8 wavelength (period) decreases (increases) slowly from 440 km (10 h) at 17 km heights to 290
9 km (14 h) at 10 km heights. The time of vertical progression of GWs is twice as long at
10 altitudes of 16-19 km which ensures GW propagation far away on a horizontal plane in the
11 LS. A sensitivity test on the horizontal propagation direction varying between 170-230° (with
12 a step of 10°) produces similar results. In conclusion, previous results derived from both
13 observations and modeling support that the mesoscale inertia GW at heights of 13-20 km is
14 generated by the jet-front system. They are consistent with the studies of Zhang (2004) and
15 Wang et al. (2009). Investigating mechanisms of generation of GWs in upper tropospheric jet-
16 front systems using a MM5 mesoscale model, these studies reveal the production of
17 mesoscale GWs lasting more than 24 h with very similar spectral characteristics ($\lambda_h=100-500$
18 km, $\lambda_v=2$ km, $\omega/f \approx 1.5$) in the troposphere and LS.

19

20 **5.4 GW induced perturbation in tracers and aerosol concentration**

21 The parcel advection method (refer to section 3.6) is applied on profiles of normalized ozone
22 and potential temperature perturbations on 27 July at 2303 UTC (Fig. 10a). The normalized
23 potential temperature perturbations are multiplied by smooth vertical profiles of coefficient
24 $R(z)$ (Fig. 10b) and superimposed on normalized ozone perturbations. The amplitudes of
25 perturbations exhibit comparable values at heights of 4-7 km and 14-24 km for perturbations
26 with vertical wavelengths <5 km. This supports the presence of GW signatures. The parcel
27 advection method is not valid at heights of 7-14 km because the vertical gradient of the ozone
28 background is very small, $R(z)$ is strongly variable with altitude, and other tropospheric
29 structures are present at 7.5 km and 12.5 km (Chane Ming et al., 2000b). The parcel method
30 also identifies GW signatures in temperature and ozone perturbation profiles on 28 July at
31 1330 UTC (Fig. 10c and 10d). In comparison with Figure 3, smaller values of normalized
32 potential temperature perturbations are observed in the LS. It means that the intensity of the
33 stratospheric GW is decreasing in the afternoon of 28 July. The Morlet CWTs of ozone and



1 temperature perturbations depict similar monochromatic structures with vertical wavelength
2 of about 1.5-3 km at heights of 10-15 km. For these two cases, GW signatures can be
3 observed in the lower troposphere above 3 km. The parcel advection method is also valid for
4 temperature and humidity mixing ratio. Figure 10e visualizes wavelike structures on specific
5 humidity profiles at heights above 3 km. The spectral densities of perturbations (Fig. 10f)
6 reveal wavelike structures of 1.5-3 km vertical wavelengths. The amplitudes of temperature
7 and specific humidity perturbations are π out of phase above 4-km height which is in
8 agreement with the parcel advection method with regards to signs of mean gradients. Thus,
9 evidence of GW signatures in ozone and humidity in the lower troposphere supports that the
10 dominant GW source is located in the jet core with an upward (downward) propagating
11 energy above (below) the source. Thus observations lead to the conclusion that the mesoscale
12 GW observed on 27 July 2013 affected the variability of stratospheric ozone-tracer fields.

13 The DWT is applied to aerosol concentrations to retrieve perturbations of aerosol
14 concentrations with vertical wavelengths of 1.6-3.2 km and the mean profile with vertical
15 wavelengths >3.2 km (Fig.11). A dominant wavelike structure with vertical wavelength of 2-
16 2.5 km is observed in the LS (15-20 km). The amplitudes of aerosol concentration
17 perturbation strongly decrease at heights of 20 km likely because of partial transmission of
18 GWs through the wind field and the presence of two layers of stratospheric aerosols with
19 different origins. The superimposition of simulated vertical perturbation aerosol upon
20 concentration perturbations profiles of the dominant mesoscale GW (Fig. 8b) indicates that
21 perturbations of aerosol concentration and simulated vertical wind are in phase at heights of
22 15-19 km (Fig. 11b). The phase relationships do not agree with the parcel advection method
23 for which perturbations should be in quadrature (refer to equation 24 in Eckermann et al.,
24 1998). Aerosols behave differently from tracer gases with production and growth processes in
25 the stratosphere. This case study suggests a possible correlation between vertical transport and
26 the distribution of aerosol concentration in the LS. In addition, large amplitudes of
27 stratospheric vertical wind with maximum values of ± 40 mms^{-1} are induced by the mesoscale
28 GW in comparison with monthly averaged amplitudes of stratospheric vertical wind of about
29 ± 5 mms^{-1} with an annual averaged of ± 1 mms^{-1} (Gryazin and Beresnev, 2011). Recent
30 theoretical studies reveal possible substantial effects of a background vertical motion on
31 stratospheric aerosol distribution. Using a four-dimensional continuity equation for particles
32 undergoing growth process, Li and Boer (2000) investigate the relative roles of condensation,
33 particle fall velocity, vertical motion, and diffusion in determining the aerosol size



1 distribution. Vertical motion could broaden the size distribution of the stratospheric
2 background aerosol which would tend to support a broader size distribution of the
3 stratospheric background aerosol in the tropics. Gryazin and Beresnev (2011) suggest that the
4 relative aerosol concentration is mostly controlled by the action of the vertical wind for
5 particles with a size $< 2.5 \mu\text{m}$. Nilsson et al. (2000) propose the use of the phase shift in
6 perturbations of aerosol concentration and vertical wind to separate the influence of turbulent
7 fluxes of aerosols from the effect of nucleation responding on waves or turbulence.
8 Perturbations should be $3\pi/4$ out of phase if nucleation dominates whereas turbulence would
9 cause perturbations to be in phase. With regard to GWs effects on cirrus clouds, the
10 combination of a mountain wave and the jet-streak GW producing a wave-induced upward
11 motion $> 10 \text{ cm s}^{-1}$ can cause ice supersaturation and trigger the formation of a cirrus cloud in
12 the UT (Spichtinger et al., 2005). A strong link has been established between GW-induced
13 mesoscale variability in vertical velocities and climate forcing by cirrus (IPCC, 2007). Haag
14 and Kärcher (2004) investigate the impact of aerosols and GWs on cirrus clouds at Northern
15 mid-latitudes. They emphasize the importance to include small-scale temperature fluctuations
16 caused by GWs for a good prediction of cloud physical properties in global models as well as
17 to represent correctly changes in GW activity in a future climate. In the present study, strong
18 modulation is also observed on amplitudes of stratospheric aerosol concentration background
19 with size class of $0.2\text{-}0.7 \mu\text{m}$ up to 60% of the background amplitude with the vertical spectral
20 characteristic of the observed stratospheric mesoscale GW.

21

22 **6 Conclusions**

23 Model studies reveal that GWs are likely to play a direct or an indirect impact on aerosol
24 processes. In addition the influence of GWs should be important during volcanically
25 quiescent periods because of low aerosol loading, especially in the tropics where the spectrum
26 of GWs and production of stratospheric aerosols are larger. A good knowledge of GW sources
27 is also crucial for determining GW spectral characteristics and intensity which will have an
28 impact on stratospheric aerosols. However, observations of effects of GWs on stratospheric
29 aerosols are still poorly documented mainly because of aerosol instrumentation limitations.
30 These observations are needed to improve aerosol modeling and to understand effects in
31 climate models. Balloon-borne optical particle counters provide direct *in situ* measurements
32 of stratospheric aerosol concentrations in several size classes. They have been shown to be
33 useful for aerosol observations during quiescent periods because of the low aerosol loading



1 and the presence of small size aerosols (Rosen et al., 1975). Performance of such instruments
2 with vertical resolution of about 5-m height has been recently improved to understand short-
3 scale variability in aerosol distribution.

4 High-resolution observations of the new balloon borne LOAC coupled with RS and
5 ozonesonde observations are shown to capture short-scale wavelike structures in the UT and
6 LS during a volcanically quiescent period during the 2013 ChArMEx. The present study
7 proposes a methodology and different complementary tools based on observations and
8 modeling, to describe GWs and to evaluate their effects on tracer constituents and the vertical
9 distribution of aerosol concentration. The methodology is fully illustrated on a case study on
10 27 July 2013 when a mesoscale inertia GW produced by the jet-front system was identified
11 during a jet-streak event. Such GWs induced strong local short-scale perturbations in the
12 amplitudes of tracer constituents, such as ozone and water vapor as well as the stratospheric
13 aerosol background layer. The simulated profile of stratospheric vertical velocity
14 perturbations produces a wave-induced upward motion with a maximum amplitude of 40
15 mms^{-1} more than ten times larger than usual amplitudes of stratospheric vertical wind. The
16 profile of wave-induced upward motion reveals to be in phase with perturbations of
17 stratospheric aerosol concentrations (size class of 0.2-0.7 μm). Besides the role of temperature
18 perturbations especially for nucleation at high frequencies, present results also support the
19 importance of GW spectral characteristics and GW-induced vertical wind perturbations in the
20 vertical aerosol distribution as also observed in formation of ice supersaturation below the
21 tropopause where cirrus clouds are observed (Spichtinger et al., 2005). In addition our study
22 lead to the conclusion that mesoscale GWs might affect significantly the mean vertical
23 distribution of stratospheric aerosol concentrations.

24 A strategy of highly-regular balloon launches has been set up using the LOAC instrument in
25 particular to investigate the short-term variations of the vertical profile of the tropospheric and
26 stratospheric aerosols using weather balloons in the framework of VOLTAIRE (VOLatils-
27 Terre, Atmosphère et Interactions-Ressources et Environnement) since December 2013.
28 Balloon-borne LOACs are launched regularly (twice per month) at Northern mid-latitudes and
29 occasionally at other latitudes. In our future research, this analysis will be extended to a
30 substantial dataset to investigate the occurrence of GW effects on LOAC vertical profiles of
31 stratospheric aerosol concentrations. These preliminary results do not exclude possible
32 threshold on GW amplitudes to trigger the GW-aerosol relation. In future, mesoscale
33 modeling with the French Meso-NH model coupled with an analytical stratospheric aerosol



1 model will enable us to highlight the different processes and the efficiency of such adiabatic
2 reversible transient events to describe the stratospheric aerosol background in particular when
3 GWs vanish.

4

5

6 **Acknowledgements**

7 The LOAC project was funded by the French National Research Agency's ANR ECOTECH.
8 The LOAC and the gondola were built by the Environnement-SA and Meteo Modem
9 companies. The balloon flights of the ChArMEx campaign were funded and performed by the
10 French Space Agency CNES. The ozone and LOAC sondes used in the campaign were
11 funded with the support of CNES, ADEME, and INSU-CNRS in the framework of the
12 MISTRALS Programme. This scientific work was financially supported by the
13 French Labex VOLTAIRE (Laboratoire d'Excellence ANR-10-LABX-100-01) and the French
14 project, StraDyVariUS ANR-13-BS06-0011-01. The satellite images were provided by
15 Météo-France/Centre de Météorologie Spatiale. Dr Stephen D. Eckermann provided
16 the GROGRAT software. The model was run on the supercomputer of the University of La
17 Réunion.

18

19 **References**

- 20 Bacmeister, J.T., Eckermann, S.D., Tsias, A., Carslaw, K.S., and Peter, T.: Fluctuations
21 induced by a spectrum of gravity waves: A comparison of parameterizations and their impact
22 on stratospheric microphysics, *J. Atmos. Sci.*, 56, 1913-1924, 1999.
- 23 Bertin, F., Campistron, B., Caccia, J. L., and Wilson, R.: Mixing processes in a tropopause
24 fold observed by a network of ST radar and lidar, *Ann. Geophysicae*, 19, 953–963, 2001.
- 25 Carslaw, K.S., Peter, T., Bacmeister, J., and Eckermann, S.D.: Widespread solid particle
26 formation by mountain waves in the Arctic stratosphere, *J. Geophys. Res.*, 104, 1827-1836,
27 1999.
- 28 Chane Ming, F., Molinaro, F., and Leveau, J.: Wavelet techniques applied to lidar signal in
29 the analysis of the middle atmosphere dynamics, *Appl. Sig. Process.*, 6(2), 95–106, 1999.
- 30 Chane Ming, F., Molinaro, F., Leveau, J., Keckhut, P., and Hauchecorne, A.: Analysis of
31 gravity waves in the tropical middle atmosphere over La Reunion Island (21°S, 55°E) with



- 1 lidar using wavelet techniques, *Ann. Geophys.*, 18, 485-498, doi:10.1007/s00585-000-0485-0,
- 2 2000a.
- 3 Chane Ming, F., Molinaro, F., Leveau, J., Keckhut, P., Hauchecorne, A., and Godin, S.:
- 4 Vertical short-scale structures in the upper tropospheric-lower stratospheric temperature and
- 5 ozone at La Reunion Island (20.8S, 55.3E), *J. Geophys. Res.*, 105, 26,857-26,866, 2000b.
- 6 Chane Ming, F., Roff, G., Robert, L., and Leveau, J.: Gravity waves characteristic over
- 7 Tromelin Island during the passage of cyclone Hudah, *Geophys. Res. Lett.*, 29, 18-1-18-4,
- 8 doi:10.1029/2003JD003489, 2002.
- 9 Chane Ming, F., Guest, F.M., and Karoly, D.J.: Gravity waves observed in temperature, wind
- 10 and ozone data over Macquarie island, *Aust. Meteor. Mag.*, 52(1), 11-21, 2003.
- 11 Chane Ming, F., Chen, Z., and Roux, F.: Analysis of gravity-waves produced by intense
- 12 tropical cyclones, *Ann. Geophys.*, 28, 531-547, doi:10.5194/angeo-28-531-2010, 2010.
- 13 Chane Ming, F., Ibrahim, C., Barthe, C., Jolivet, S., Keckhut, P., Liou, Y.A., and
- 14 Kuleshov, Y.: Observation and a numerical study of gravity waves during tropical cyclone
- 15 Ivan (2008), *Atmos. Chem. Phys.*, 14, 641-658, doi:10.5194/acp-14-641-2014, 2014.
- 16 Clark, A.J., Schaffer, C.J., Gallus, Jr W.A., and Johnson-O'Mara, K.: Climatology of storm
- 17 reports relative to upper-level jet streaks, *Wea. Forecasting*, 24, 1032-1051, 2009.
- 18 Cunningham, P., and Keyser, D.: *Encyclopedia of Atmospheric Sciences*, Academic Press,
- 19 1043-1055, 2003.
- 20 Deshler, T.: A review of global stratospheric aerosol: measurements, importance, life cycle,
- 21 and local stratospheric aerosol, *Atmos. Res.*, 90, 223-232, 2008
- 22 Domingues, M.O., Mendes, O., and Mendes da Costa, A.: On wavelet techniques in
- 23 atmospheric sciences, *Adv. Space Res.*, 35,831-842, 2005.
- 24 Eckermann, S.D.: Hodographic analysis of gravity waves: relationships among Stokes
- 25 parameters, rotary spectra and cross- spectral methods, *J. Geophys. Res.*, 101, 19169–19174,
- 26 1996.
- 27 Eckermann, S.D., and Marks, C.J.: GROGRAT: A new model of the global propagation and
- 28 dissipation of atmospheric gravity waves, *Adv. Space Res.*, 20, 1253-1256, 1997.
- 29 Eckermann, S.D., Gibson-Wilde, D.E., and Bacmeister, J.T.: Gravity wave perturbations of
- 30 minor constituents: A parcel advection methodology, *J. Atmos. Sci.*, 55, 3521-3539, 1998.



- 1 Ern, M., Preusse, P., Alexander, M.J., and Warner, C.D.: Absolute values of gravity wave
2 momentum flux derived from satellite data, *J. Geophys. Res.*, 109, D20103,
3 doi:10.1029/2004JD004752, 2004.
- 4 Ern, M., Ploeger, F., Preusse, P., Gille, J.C., Gray, L.J., Kalisch, S., Mlynczak, M.G., Russell,
5 J.M., and Riese, M.: Interaction of gravity waves with the QBO: A satellite perspective, *J.*
6 *Geophys. Res.*, 119, 2329-2355, doi:10.1002/2013JD020731, 2014.
- 7 Faber, A., Llamedo, P., Schmidt, T., de la Torre, A., and Wickert, J.: On the determination of
8 gravity wave momentum flux from GPS radio occultation data, *Atmos. Meas. Tech.*, 6, 3169-
9 3180, doi:10.5194/amt-6-3169-2013, 2013.
- 10 Fan, J., Yuan, T., Comstock, J. M., Ghan, S., Khain, A., Leung, L. R., Li, Z., Martins, V. J.,
11 and Ovchinnikov, M.: Dominant role by vertical wind shear in regulating aerosol effects on
12 deep convective clouds, *J. Geophys. Res.*, 114, D22206, doi:10.1029/2009JD012352, 2009.
- 13 Fritts, D.C., and Alexander, M.J.: Gravity wave dynamics and effects in the middle
14 atmosphere, *Rev. Geophys.*, 41, 1003, doi:10.1029/2001RG000106, 2003.
- 15 Geller, M.A., Alexander, M.J., Love, P.T., Bacmeister, J., Ern, M., Hertzog, A., Manzini, E.,
16 Preusse, P., Sato, K., Scaife, A.A., and Zhou, T.: A comparison between gravity wave
17 momentum fluxes in observations and climate models, *J. Climate*, 26, 6383-6405, 2013.
- 18 Gill, A. E.: *Atmosphere-Ocean Dynamics*, Academic Press, 131-139, 1982.
- 19 Gryazin, V., and Beresnev, S. A.: Influence of vertical wind on stratospheric aerosol
20 transport, *Meteor. Atmos. Phys.*, 110, 151-162, 2011.
- 21 Guest, F.M., Reeder, M.J., Marks, C.J., and Karoly, D.J.: Inertia gravity waves observed in
22 the lower stratosphere over Macquarie Island, *J. Atmos. Sci.*, 57, 737-752, 2000.
- 23 Guest, F.M., Reeder, M.J., and Chane Ming, F.: Analyses of inertia-gravity waves in upper-air
24 soundings made from Macquarie Island, *Aust. Met. Mag.*, 51, 107-15, 2002.
- 25 Haag, W., and Bärcher, B.: The impact of aerosols and gravity waves on cirrus clouds at
26 midlatitudes, *J. Geophys. Res.*, 109, D12202, doi:10.1029/2004JD004579, 2004.
- 27 Hamill, P., Jensen, E.J., Russell, P.B., and Bauman, J.J.: The life cycle of stratospheric
28 aerosol particles, *Bull. Am. Meteorol. Soc.*, 7, 1395-1410, 1997.



- 1 Hertzog, A., Vial, F., Mechoso, C.R., Basdevant, C., and Cocquerez, P.: Quasi-lagrangian
2 measurements in the lower stratosphere reveal an energy peak associated with near-inertial
3 waves, *Geophys. Res. Lett.*, 29, 1229, doi:10.1029/2001GL014083, 2002.
- 4 Hindley, N.P., Wright, C.J., Smith, N.D., and Mitchell, N.J.: The southern stratospheric
5 gravity-wave hot spot: individual waves and their momentum fluxes measured by COSMIC
6 GPS-RO, *Atmos. Chem. Phys.*, 15, 7797-7818, doi:10.5194/acp-15-7797-2015, 2015.
- 7 Hobbs, P.V.: *Aerosol-cloud-climate interactions*, Academic Press, 1993.
- 8 Hommel, R., Timmreck, C., Giorgetta, M. A., and Graf, H. F.: Quasi-biennial oscillation of
9 the tropical stratospheric aerosol layer, *Atmos. Chem. Phys.*, 15, 5557-5584, doi:10.5194/acp-
10 15-5557-2015, 2015.
- 11 IPCC 2007: Contribution of Working Group I to the Fourth Assessment Report of the
12 Intergovernmental Panel on Climate Change, Cambridge University Press, Cambridge, United
13 Kingdom and New York, NY, USA, 2007.
- 14 Junge, C.E., Changnon, C.W., and Manson, J.E.: Stratospheric aerosols, *J. Meteor.*, 18, 81-
15 108, 1961.
- 16 Koch, S., and O'Handley, C.: Operational forecasting and detection of mesoscale gravity
17 waves, *Wea. Forecasting*, 12, 253-281, 1997.
- 18 Komhyr, W.: Electrochemical concentration cells for gas analysis, *Ann. Geophys.*, 25, 203-
19 210, 1969.
- 20 Kumar, P., and Foufoula-Georgiou, E.: A new look at rainfall fluctuations and scaling
21 properties of spatial rainfall using orthogonal wavelets, *J. Appl. Meteor.*, 32,209-222, 1993.
- 22 Kursinski, E.R., Hajj, G.A., Schofield, J.T., Linfoeld, R.P., and Hardy, K.R.: Observing
23 Earth's atmosphere with radio occultation measurements using the Global Positioning
24 System, *J. Geophys. Res.*, 102, 23429-23465, doi:10.1029/97JD0156, 1997.
- 25 Lange, M., and Jacobi, C.: *Analysis of gravity waves from radio occultation measurements*,
26 Springer Berlin, 479-484, 2003.
- 27 Li, J., and Boer, G. J.: The continuity equation for the stratospheric aerosol and its
28 characteristic curves, *J. Atmos. Sci.*, 57, 442-451, 2000.
- 29 Lin, Y.L.: *Mesoscale dynamics*, Cambridge University Press, 379-437, 2007.



- 1 Liou, Y.A., Pavelyev, A.G., Wicker, J., Liu, S.F., Pavelyev, A.A., Schmidt, T., and Igarashi,
2 K.: Application of GPS radio occultation method for observation of the internal waves in the
3 atmosphere, *J. Geophys. Res.*, 111, D06104, doi:10.1029/2005JD005823, 2006.
- 4 Lurton, T., Renard, J.B., Vignelles, D., Jeannot, M., Akiki, R., Mineau, J.L., and Tonnelier,
5 T.: Light scattering at small angles by atmospheric irregular particles: modelling and
6 laboratory 15 measurements, *Atmos. Meas. Tech.*, 7, 931-939, doi:10.5194/amt-7-931-2014,
7 2014.
- 8 Marks, C.J., and Eckermann, S.D.: A three-dimensional nonhydrostatic ray-tracing model for
9 gravity waves: Formulation and preliminary results for the middle atmosphere, *J. Atmos. Sci.*,
10 52, 1959-1984, 1995.
- 11 Matsumura, T., Hayashi, M., Fujiwara, M., Matsunaga, K., Yasui, M., Saraspriya, S., Manik,
12 T., Suropto, A.: Observations of Stratospheric Aerosols by Balloon-borne Optical Particle
13 Counter at Bandung, Indonesia, *J. Meteor. Soc. Jap.*, 79, 709-718, 2001.
- 14 Murphy, D.M., Cziczo, D.J., Hudson, P.K., and Thomson, D.S.: Carbonaceous material in
15 aerosol particles in the lower stratosphere and tropopause region, *J. Geophys. Res.*, 112,
16 doi:10.1029/2006JD007297, 2007.
- 17 Nilsson, E.D., Pirjola, L., and Kulmala, M.: The effect of atmospheric waves on aerosol
18 nucleation and size distribution, *J. Geophys. Res.*, 105, 19,917-19,926, 2000.
- 19 O'Sullivan, D., and Dunkerton, T.J.: Generation of inertia-gravity waves in a simulated life
20 cycle of baroclinic instability, *J. Atmos. Sci.*, 52, 3695-3716, 1995.
- 21 Plougonven, R., and Zhang, F.: Internal gravity waves from atmospheric jets and fronts, *Rev.*
22 *Geophys.*, 52, doi:10.1002/2012RG000419, 2014.
- 23 Plumb, R.A., Waugh, D.W., Atkinson, R.J., Newman, P.A., Lait, L.R., Schoeberl, M.R.,
24 Browell, E.V., Simmons, A.J., and Loewenstein, M.: Intrusions into the lower stratospheric
25 Arctic vortex during the winter of 1991/92, *J. Geophys. Res.*, 99, 1089-1105, 1994.
- 26 Pollicott, M., and Howard, W.: How Smooth is Your Wavelet? Wavelet Regularity via
27 Thermodynamic Formalism, *Communications in Mathematical Physics*, 281, 1-21, 2008.
- 28 Preusse, P., Dornbrack, A., Eckermann, S. D., Riese, M., Schaeler, B., Bacmeister, J. T.,
29 Broutman, D., and Grossmann, K. U.: Space-based measurements of stratospheric mountain
30 waves by CRISTA, *J. Geophys. Res.*, 107, 8178, doi:10.1029/2001JD000699, 2002.



- 1 Preusse, P., Eckermann, S.D., Ern, M., Oberheide, J., Picard, R.H., Roble, R.G., Riese,
2 M., Russell, J.M., and Mlynczak, M.G.: Global ray tracing simulations of the SABER gravity
3 wave climatology, *J. Geophys. Res.*, 114, D08126, doi:10.1029/2008JD011214, 2009.
- 4 Preusse, P., Ern, M., Bechtold, P., Eckermann, S.D., Kalisch, S., Trinh, Q.T., and Riese, M.:
5 Characteristics of gravity waves resolved by ECMWF, *Atmos. Chem. Phys.*, 14, 10483-
6 10508, doi:10.5194/acp-14-10483-2014, 2014.
- 7 Randel, W., Boville, B.A., and Gille, J.C.: Observations of planetary mixed Rossby-gravity
8 waves in the upper stratosphere, *J. Atmos. Sci.*, 47, 3092-3099, doi:10.1175/1520-0469, 1990.
- 9 Renard, J.B., Dulac, F., Berthet, G., Lurton, T., Vignelles, D., Jégou, F., Tonnelier, T.,
10 Thauray, C., Jeannot, M., Couté, B., Akiki, R., Verdier, N., Mallet, M., Gensdarmes, F.,
11 Charpentier, P., Duverger, V., Dupont, J.V., Mesmin, S., Elias, T., Crenn, V., Sciare, J.,
12 Giacomoni, J., Gobbi, M., Hamonou, E., Olafsson, H., Dagsson-Waldhauserova, P., Camy-
13 Peyret, C., Mazel, C., Décamps, T., Piringer, M., Surcin, J., and Daugeron, D.: LOAC: a
14 small aerosol optical counter/sizer for ground-based and balloon measurements of the size
15 distribution and nature of atmospheric particles – Part 1: Principle of measurements and
16 instrument evaluation, *Atmos. Meas. Tech. Discuss.*, 8, 9993-10056, doi:10.5194/amtd-8-
17 9993-2015, 2015.
- 18 Renard, J.B., Dulac, F., Berthet, G., Lurton, T., Vignelles, D., Jégou, F., Tonnelier, T.,
19 Thauray, C., Jeannot, M., Couté, B., Akiki, R., Verdier, N., Mallet, M., Gensdarmes, F.,
20 Charpentier, P., Duverger, V., Dupont, J.V., Mesmin, S., Elias, T., Crenn, V., Sciare, J.,
21 Giacomoni, J., Gobbi, M., Hamonou, E., Olafsson, H., Dagsson-Waldhauserova, P., Camy-
22 Peyret, C., Mazel, C., Décamps, T., Piringer, M., Surcin, J., and Daugeron, D.: LOAC: a
23 small aerosol optical counter/sizer for ground-based and balloon measurements of the size
24 distribution and nature of atmospheric particles – Part 2: First results from balloon and
25 unmanned aerial vehicle flights, *Atmos. Meas. Tech. Discuss.*, 8, 10057-10096,
26 doi:10.5194/amtd-8-10057-2015, 2015.
- 27 Ravetta, F., Ancellet, G., Kowol-Santen, J., Wilson, R., and Nedeljkovic, D.: Ozone,
28 temperature and wind field measurements in a tropopause fold: comparison with a mesoscale
29 model simulation, *Mon. Wea. Rev.*, 127, 2641–2653, 1999.
- 30 Rose, S.F., Hobbs, P.V., Locatelli, J.D., and Stoelinga, M.T.: A 10-yr climatology relating the
31 locations of reported tornadoes to the quadrants of upper-level jet streaks, *Wea. Forecasting*,
32 19, 301-309, 2004.



- 1 Shapiro, M.A.: Turbulent mixing within tropopause folds as a mechanism for the exchange of
2 chemical constituents between the stratosphere and troposphere, *J. Atmos. Sci.*, 37, 994-1004,
3 1980.
- 4 Shutts, G.J., and Vosper, S.B.: Stratospheric gravity waves revealed in NWP model forecasts,
5 *Q. J. Roy. Meteorol. Soc.*, 137, 303-317, doi:10.1002/qj.7, 2011.
- 6 Smit, H., Straeter, W., Johnson, B., Oltmans, S., Davies, J., Tarasick, D., Hoegger, B., Stuebi,
7 R., Schmidlin, F., Northam, T., Thompson, A., Witte, J., Boyd, I., and Posny, F.: Assessment
8 of the performance of ECC-ozonesondes under quasi-flight conditions in the environmental
9 simulation chamber: Insights from the Juelich Ozone Sonde Intercomparison Experiment
10 (JOSIE), *J. Geophys. Res.*, 112, D19, doi:10.1029/2006JD007308, 2007.
- 11 Smit, H.: the Panel for the Assessment of Standard Operating Procedures for Ozonesondes
12 (ASOPOS). Quality assurance and quality control for ozone sonde measurements in GAW,
13 GAW Report no. 201, World Meteorological Organization,
14 http://www.wmo.int/pages/prog/arep/gaw/documents/GAW_201.pdf, 2011.
- 15 Solomon, S., Daniel, J.S., Neely, III R.R., Vernier, J.P., Dutton, E.G., and Thomason, L.W.:
16 The persistently variable "Background" stratospheric aerosol layer and global climate change,
17 *Science*, 333, 866-870, doi:10.1126/science.1206027, 2011.
- 18 SPARC Report No. 4: SPARC Assessment of Stratospheric Aerosol Properties (ASAP), L.
19 Thomason and Th. Peter (Eds.), WCRP-124, WMO/TD SPARC, 2006.
- 20 Spichtinger, P., Gierens, K., and Dörnbrack, A.: Formation of ice supersaturation by
21 mesoscale gravity waves, *Atmos. Chem. Phys.*, 5, 1243-1255, doi:10.5194/acp-5-1243-2005,
22 2005.
- 23 Stohl, A., Wotawa, G., Seibert, P., and Kromp-Kolb, H.: Interpolation errors in wind fields as
24 a function of spatial and temporal resolution and their impact on different types of kinematic
25 trajectories, *J. Appl. Meteor.*, 34, 2149-2165, 1995.
- 26 Stohl, A., Forster, C., Frank, A., Seibert, P., and Wotawa, G.: Technical note: The Lagrangian
27 particle dispersion model FLEXPART version 6.2, *Atmos. Chem. Phys.*, 5, 2461-2474,
28 doi:10.5194/acp-5-2461-2005, 2005.
- 29 Strang, G., and Nguyen, T.: *Wavelets and Filter Banks*, Wellesley-Cambridge Press, 103-
30 259, 1996.



- 1 Teitelbaum, H., Ovarlez, J., Kelder, H., and Lott, F.: Some observations of gravity-wave-
2 induced structure in ozone and water vapour during EASOE, *Geophys. Res. Lett.*, 21, 1483-
3 1486, 1994.
- 4 Thomas, L., Worthington, R. M., and McDonald, A. J.: Inertia gravity waves in the
5 troposphere and lower stratosphere associated with a jet stream exit region, *Ann. Geophys.*,
6 17, 115– 121, 1999.
- 7 Tsuda, T., Nishida, M., Rocken, C., and Ware, R.H.: A global morphology of gravity wave
8 activity in the stratosphere revealed by the GPS occultation data (GPS/MET), *J. Geophys.*
9 *Res.*, 105, 7257-7273, 2000.
- 10 Uccellini, L.W., and Koch, S.E.: The synoptic setting and possible energy sources for
11 mesoscale wave disturbances, *Mon. Wea. Rev.*, 115, 721-729, 1987.
- 12 Vaughan, G., Jenkins, D. B., Thomas, L., Wareing, D. P., Farrington, M.: Dynamical
13 influences on stratospheric aerosols observed at Aberystwyth in early 1983, *Tellus*, 39B, 398–
14 411, 1987.
- 15 Vincent, R.A., Allen, S.J., and Eckermann, S.D.: Gravity wave parameters in the lower
16 stratosphere. Gravity wave processes: Their parameterization in global climate models,
17 Springer-Verlag, 7-25, 1997.
- 18 Walker, J.S.: *A Primer on Wavelets and Their Scientific Applications*, Chapman & Hall/CRC
19 Press, 318pp, 2008.
- 20 Wang, L., and Alexander, M.J.: Global Estimates of gravity wave parameters from GPS radio
21 occultation temperature data, *J. Geophys. Res.*, 115, D21122, doi:10.1029/2010JD013860,
22 2010.
- 23 Wang, S., Zhang, F., and Snyder, C.: Generation and propagation of inertia–gravity waves
24 from vortex dipoles and jets, *J. Atmos. Sci.*, 66, 1294-1314, doi:10.1175/2008JAS2830.1,
25 2009.
- 26 Xu, J., Smith, A.K., and Brasseur, G.: The effects of gravity waves on distributions of
27 chemically active constituents in the mesopause region, *J. Geophys. Res.*, 105, 26,593-26,
28 602, doi:10.1029/2000JD900446, 2000.
- 29 Zahn, A., Brenninkmeijer, C.A.M., Maiss, M., Scharffe, D.H., Crutzen, P.J., Hermann,
30 M., Heintzenberg, J., Wiedensohler, A., Giusten, H., Heinrich, G., Fischer, H., Cuijpers,
31 J.W.M., van Velthoven, P.F.J.: Identification of extratropical two-way troposphere-



- 1 stratosphere mixing based on CARIBIC measurements of O₃, CO, and ultrafine particles, J. Geophys. Res., 105, 1527-1535, 2000.
- 2
- 3 Zhang, F.: Generation of mesoscale gravity waves in upper-tropospheric jet-front systems, J. Atmos. Sci., 61(4), 440-457, 2004.
- 4
- 5
- 6



Table 1. Characteristics of GWs on 27 July at 2303 UTC above Ile du Levant using a hodograph analysis and combined conventional methods (grey cells) on observed and simulated (marked by *) profiles. Height: altitude range, E_t : total energy density, E_k : kinetic energy, E_p : potential energy, Φ : direction of horizontal wave propagation (clockwise from north), λ_v , λ_h : vertical and horizontal wavelengths, ω/f : intrinsic frequency/inertial frequency, T : period. Parentheses denote standard deviation. Units are in brackets.

Heights (km)	E_t ($J.kg^{-1}$)	E_k ($J.kg^{-1}$)	E_p ($J.kg^{-1}$)	λ_v (km)	λ_h (km)	ω/f	T (h)	Φ ($^\circ$)
3-7	11.3	7.6	3.7	2.6	451 (23) 204 (10) 161 (20)	1.2 (0.1) 1.6 (0.1)	14.6 (0.9) 11.1 (0.5) 9.6 (0.2)	236 (12)
13-20	16.6	12.3	4.3	2.6	483.5 (108.7)	1.5 (0.1)	11.5 (1.16)	220 (29)
20-23	5.4	4.6	0.8	2	850 (34) 1260 (241)	1.1 (0.1)	16.4 (0.6)	95 (16)
3-7*				2.6	202.3 (146.9)	1.8 (0.4)	10 (2.7)	203.4 (11.9)
13-20*	15.2	10.5	4.68	2.6	486.5 (69.8)	1.5 (0.1)	11 (0.86)	204 (2.5)
13-20	15.7	11.3	4.4	2.6	510	1.47	12	204
20-26	6.1	5.1	1	2	1300 440	1.12	15.6	112
13-20*	15.5	10.5	5.1	2.4	370	1.68	11	205 242



Figure captions

Figure 1. 50-m interpolated vertical profiles of aerosol concentration (cm^{-3}) with diameters 0.2-50 μm above Minorca Island (39.99°N, 4.25°E) **(a-b)** on 19 June at 1341 UTC and 28 June at 0530 UTC respectively, and above Ile du Levant (43.02°N, 6.46°E) **(c-d)** on 27 July at 2303 UTC and 3 August at 1056 UTC during the ChArMEx campaign in summer 2013.

Figure 2. **(a)** Latitude-longitude distribution of wind speed (ms^{-1}) at 300-hPa on 27 July at 1200 UTC (color scale: red relatively high values, blue relatively low values). Wind speed exceeds $>50 \text{ ms}^{-1}$ above west of Portugal (yellow dashed line), solid lines indicate geopotential height (m) at 500-hPa derived from ECMWF operational analyses on 27 July at 1200 UTC, **(b)** Backward air mass trajectories using the FLEXTRA model starting at every 1-km height from levels of 15-25 km above Ile du Levant during 10 days from 27 July at 2300 UTC, interval between 2 triangles corresponds to a duration of 24 h. Color indicates altitude (km).

Figure 3. Filtered vertical profiles of temperature ($^{\circ}\text{C}$), potential temperature ($^{\circ}\text{K}$), zonal and meridional winds (ms^{-1}), ozone, LOAC aerosol concentration (cm^{-3}) of 0.2-0.7 μm size classes **(a, b, c, g, h, i)** and perturbations **(d, e, f, j, k, l)** on 27 July at 2303 UTC above Ile du Levant (43.02°N, 6.46°E). Solid blue (red) line visualizes filtered (background) profile. The prime symbol (') means perturbations.

Figure 4. Morlet CWT (given in units of physical unit² km^{-1}) on the left panels of perturbations of **(a)** normalized potential temperature, **(b) (c)** horizontal wind components u and v (ms^{-1}), respectively, and **(d)** ozone (ppmv) and **(e)** aerosol concentration (cm^{-3}) of size 0.2-0.7 μm size classes. Perturbations are visualized on the right panels. Color scale: red relatively high values, blue relatively low values. **(f)** Normalized fast Fourier transform of normalized potential temperature, normalized temperature, horizontal wind (ms^{-1}) and ozone (ppmv) and aerosol concentration (cm^{-3}) perturbations at heights of 15-23 km.

Figure 5. Vertical velocity (Pa s^{-1}) at 50 hPa in the lower stratosphere derived from ECMWF analyses on 27 July 2013 at 1800 UTC. The star symbol locates Ile du Levant. **(b)** Spectral density ($\text{Pa}^2 \text{ s}^{-2} \text{ km}^{-1}$) as a function of latitudes for horizontal wavelengths (km) in east-west direction $\lambda_x < 500 \text{ km}$, 500-1000 km and 1000-2000 km, **(c)** spectral density distribution at latitudes ranged between 42°N and 52°N and **(d)** spectral density at the latitudes of 42-48°N and 46°N.



Figure 6. **(a)** Location of GPS RO COSMIC data on 26, 27, 28 and 29 July 2013 marked with x, +, triangle, square symbols respectively. The black dot locates Ile du Levant. Numbers near markers indicate hours (UTC) of profiles from which **(b)** spectral densities ($C^2 \text{ km}^{-1}$) of GPS RO temperature perturbations ($^{\circ}\text{C}$) are calculated for modes with vertical wavelengths $< 5 \text{ km}$ at altitudes of 10-20 km at heights of 10-20 km at longitudes of 2.5° - 6°E and latitudes of 40 - 50°N on 26, 27, 28 and 29 July 2013 (upper panel to lower panel respectively).

Figure 7. **(a)** Vertical profiles of temperature ($^{\circ}\text{C}$) and perturbations ($^{\circ}\text{C}$) on the left and right panels respectively from RS and RO data on 27 July at 2303, 28 July 2013 at 0200 and 1200 UTC respectively. Morlet CWT (left panel) of temperature perturbations (right panel) of RO data on 28 July 2013 at **(b)** 0200 UTC and **(c)** 1200 UTC respectively. **(d)** Cross wavelet spectrum ($C^4 \text{ km}^{-2}$) on 28 July 2013 at 0200 UTC and 1200 UTC and corresponding horizontal wavelength (km) as a function of altitudes for vertical wavelengths between 2.5 km (blue solid line) and 3 km (red solid line). Color scale: red relatively high values, blue relatively low values.

Figure 8. **(a)** Observed (blue solid line) and simulated temperature (green solid line) in units of $^{\circ}\text{C}$ (left panel) respectively on 27 July at 2303 UTC. Same as the left panel but for horizontal wind profiles (ms^{-1}). Red solid lines indicate the observed mean profile. **(b)** Simulated perturbation profiles using GW simplified linear wave polarization relations. U' , V' and T' are zonal wind (ms^{-1}), meridional wind (ms^{-1}) and temperature ($^{\circ}\text{C}$) perturbations respectively.

Figure 9. Backward rays from Ile du Levant launched at 19 km height on 28 July at 0000 UTC onto **(a)** georeferenced infrared GMS-3 image and **(b)** altitude-latitude cross section (color scale: red relatively high values, blue relatively low values) of zonal wind (ms^{-1}) at longitude of 0.0 E on 27 July at 1200 UTC. **(c)** Evolution of horizontal wavelength in units of km (solid line), ω/f (dash-dot line) and time in units of h (dashed line) as a function of altitude (km).

Figure 10. **(a)** Normalized perturbations of the temperature and the ozone mixing ratio for the vertical wavelength bandwidth of 1.2-4.8 km using DWT. Temperature perturbation ($^{\circ}\text{C}$) profile has been multiplied by the factor $R(z)$ **(b)** defined in section 3.6. **(c)** and **(d)** Morlet CWT (left panels) of normalized temperature and ozone concentration (ppmv) perturbations (right panels) on 28 July at 1330 UTC (color scale: red relatively high values, blue relatively low values). **(e)** Specific humidity (gkg^{-1}) and perturbations on 27 July at 2303 UTC and 28



July at 1330 UTC at heights of 3-11 km, and **(f)** corresponding normalized spectral density of specific humidity.

Figure 11. Vertical profiles of **(a)** aerosol concentration (cm^{-3}) and **(b)** aerosol (size class: 0.2-50 μm) perturbations with 1.6-3.2 km vertical wavelengths and simulated vertical wind perturbations (ms^{-1}) on 27 July at 2303 UTC. On left panel, black (red) solid line corresponds to raw (background) profile (cm^{-3}). The sum of the background profile and GW perturbations is drawn as green solid line.

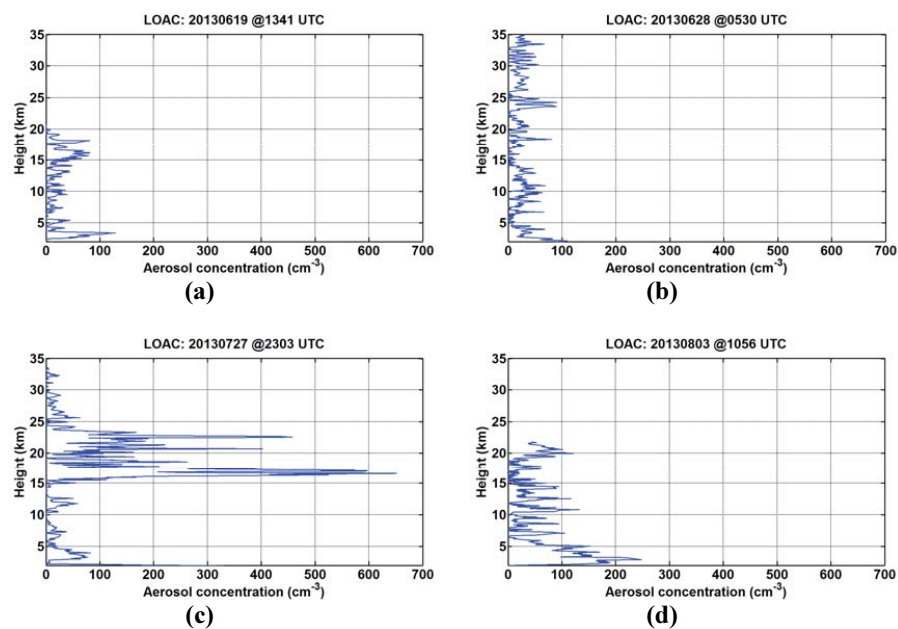
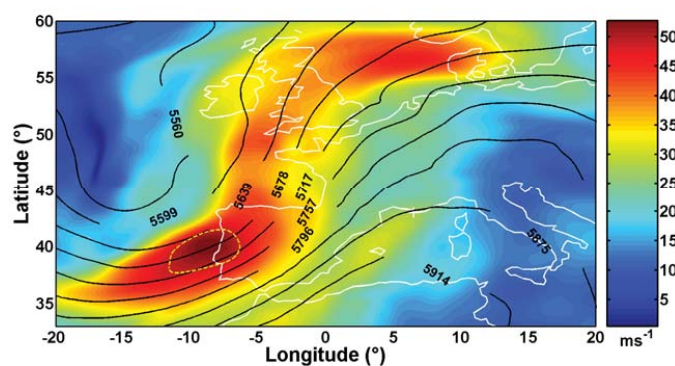
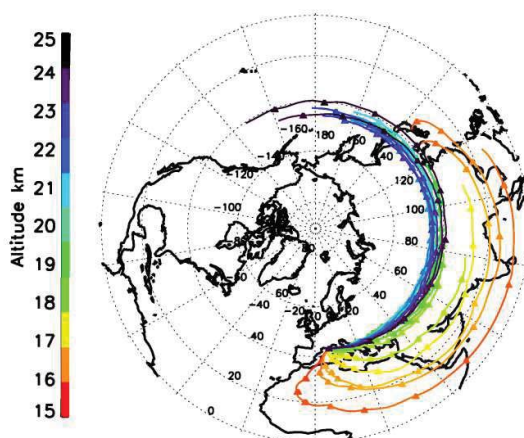


Figure 1. 50-m interpolated vertical profiles of aerosol concentration (cm⁻³) with diameters 0.2-50 μm above Minorca Island (39.99°N, 4.25°E) **(a-b)** on 19 June at 1341 UTC and 28 June at 0530 UTC respectively, and above Ile du Levant (43.02°N, 6.46°E) **(c-d)** on 27 July at 2303 UTC and 3 August at 1056 UTC during the ChArMEx campaign in summer 2013.



(a)



(b)

Figure 2. **(a)** Latitude-longitude distribution of wind speed (ms^{-1}) at 300-hPa on 27 July at 1200 UTC (color scale: red relatively high values, blue relatively low values). Wind speed exceeds $>50 \text{ ms}^{-1}$ above west of Portugal (yellow dashed line), solid lines indicate geopotential height (m) at 500-hPa derived from ECMWF operational analyses on 27 July at 1200 UTC, **(b)** Backward air mass trajectories using the FLEXTRA model starting at every 1-km height from levels of 15-25 km above Ile du Levant during 10 days from 27 July at 2300 UTC, interval between 2 triangles corresponds to a duration of 24 h. Color indicates altitude (km).

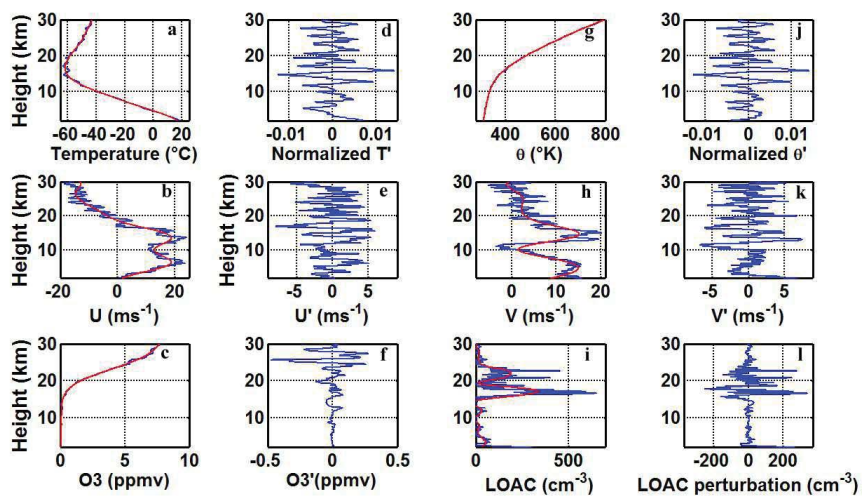


Figure 3. Filtered vertical profiles of temperature ($^{\circ}\text{C}$), potential temperature ($^{\circ}\text{K}$), zonal and meridional winds (ms^{-1}), ozone, LOAC aerosol concentration (cm^{-3}) of 0.2-0.7 μm size classes (**a**, **b**, **c**, **g**, **h**, **i**) and perturbations (**d**, **e**, **f**, **j**, **k**, **l**) on 27 July at 2303 UTC above Ile du Levant (43.02°N , 6.46°E). Solid blue (red) line visualizes filtered (background) profile. The prime symbol ($'$) means perturbations.

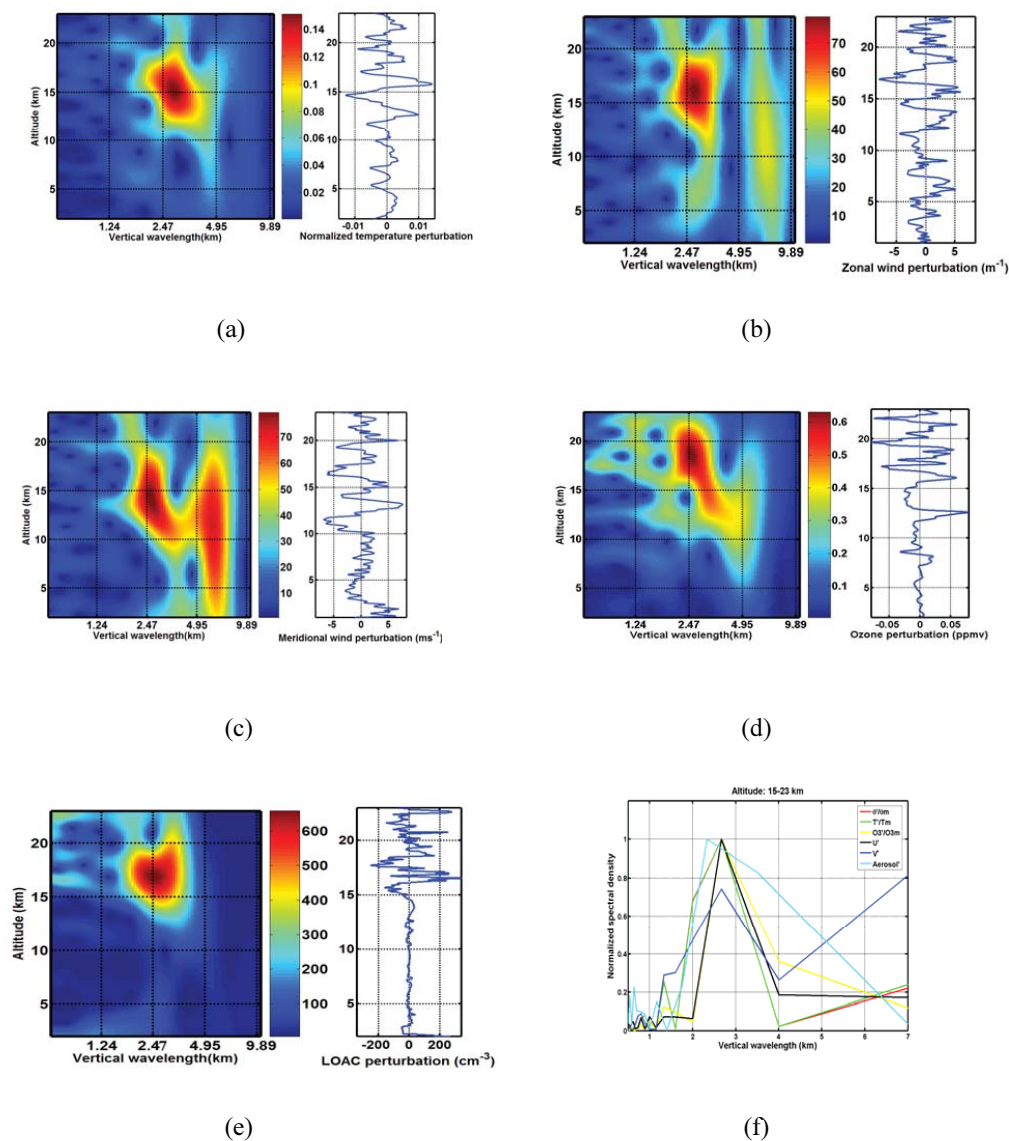


Figure 4. Morlet CWT (given in units of physical unit² km⁻¹) on the left panels of perturbations of **(a)** normalized potential temperature, **(b)** **(c)** horizontal wind components u and v (ms⁻¹), respectively, and **(d)** ozone (ppmv) and **(e)** aerosol concentration (cm⁻³) of size 0.2-0.7 μ m size classes. Perturbations are visualized on the right panels. Color scale: red relatively high values, blue relatively low values. **(f)** Normalized fast Fourier transform of normalized potential temperature, normalized temperature, horizontal wind (ms⁻¹) and ozone (ppmv) and aerosol concentration (cm⁻³) perturbations at heights of 15-23 km.

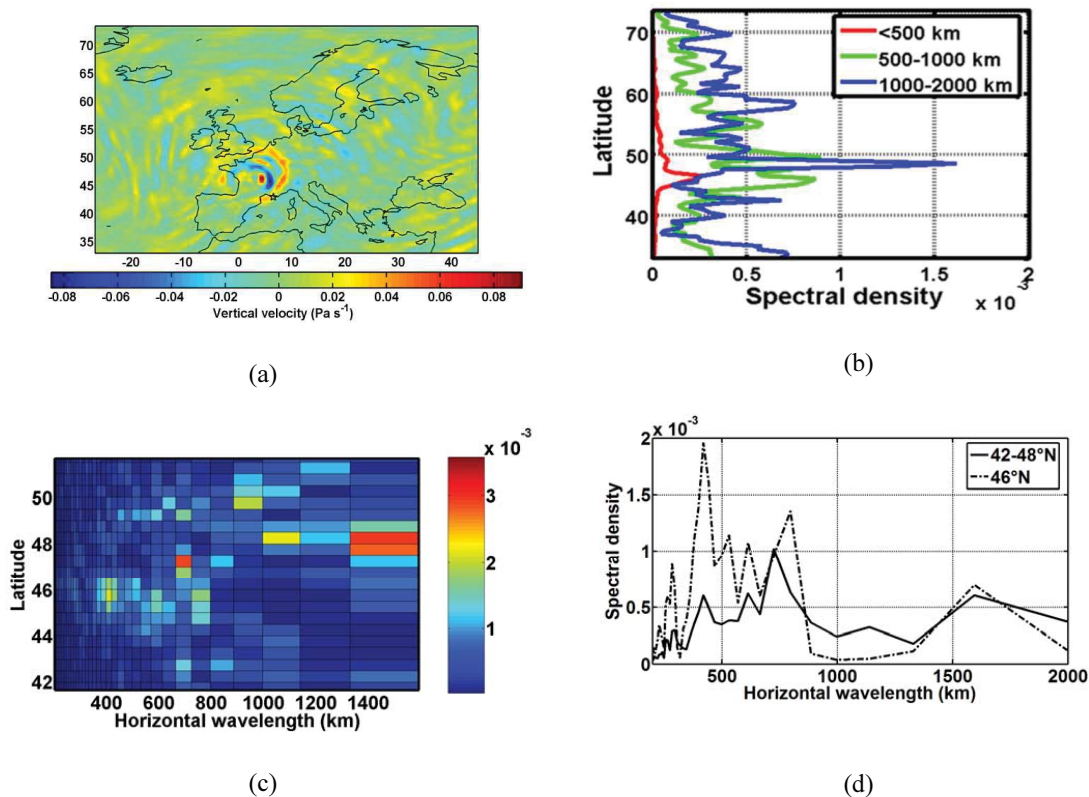
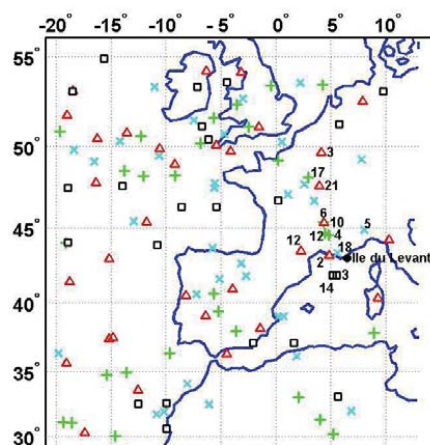
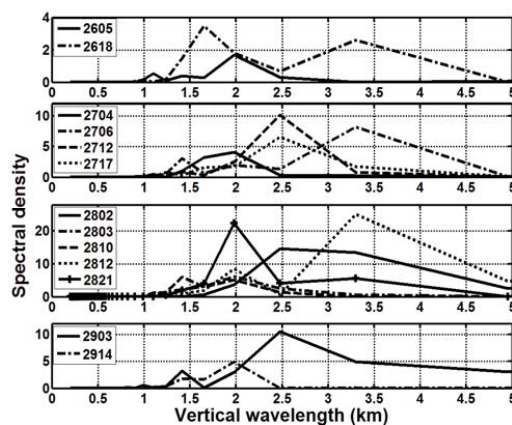


Figure 5. **(a)** Vertical velocity (Pa s^{-1}) at 50 hPa in the lower stratosphere derived from ECMWF analyses on 27 July 2013 at 1800 UTC. The star symbol locates Ile du Levant. **(b)** Spectral density ($\text{Pa}^2 \text{s}^{-2} \text{km}^{-1}$) as a function of latitudes for horizontal wavelengths (km) in east-west direction $\lambda_x < 500$ km, 500-1000 km and 1000-2000 km, **(c)** spectral density distribution at latitudes ranged between 42°N and 52°N and **(d)** spectral density at the latitudes of 42-48°N and 46°N.



(a)



(b)

Figure 6. (a) Location of GPS RO COSMIC data on 26, 27, 28 and 29 July 2013 marked with x, +, triangle, square symbols respectively. The black dot locates Ile du Levant. Numbers near markers indicate hours (UTC) of profiles from which (b) spectral densities ($C^2 \text{ km}^{-1}$) of GPS RO temperature perturbations ($^{\circ}\text{C}$) are calculated for modes with vertical wavelengths $< 5 \text{ km}$ at altitudes of 10–20 km at heights of 10–20 km at longitudes of 2.5°–6°E and latitudes of 40–50°N on 26, 27, 28 and 29 July 2013 (upper panel to lower panel respectively).

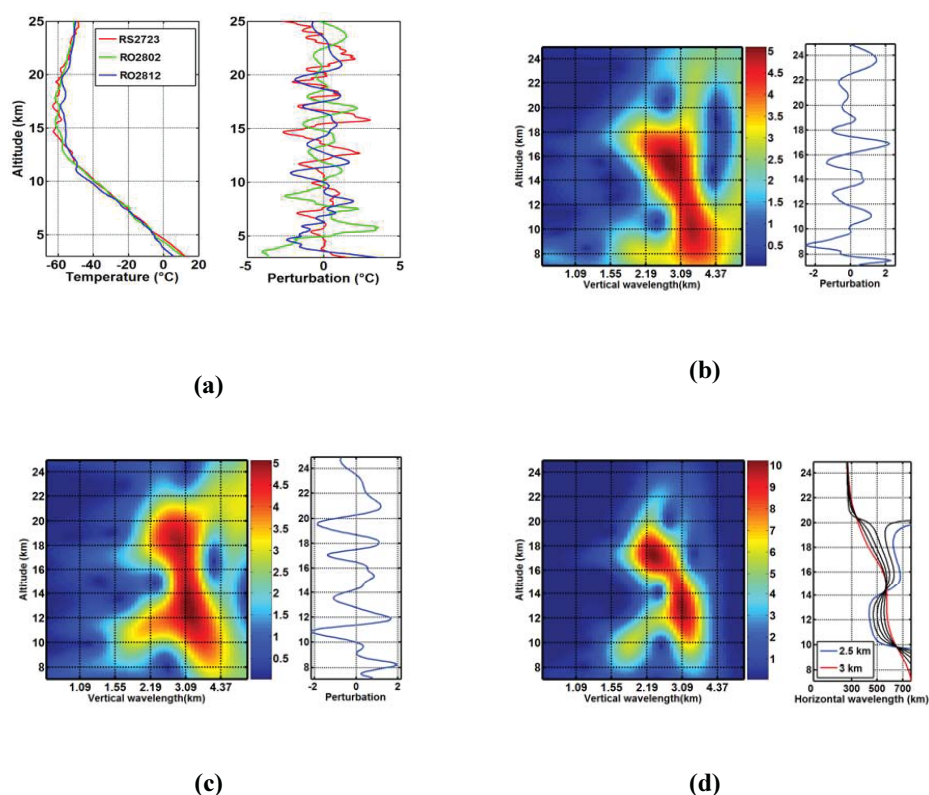
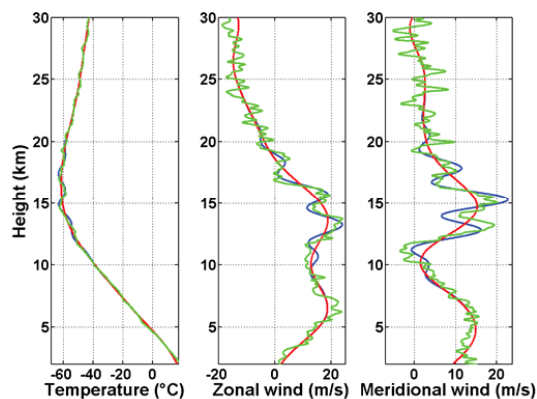
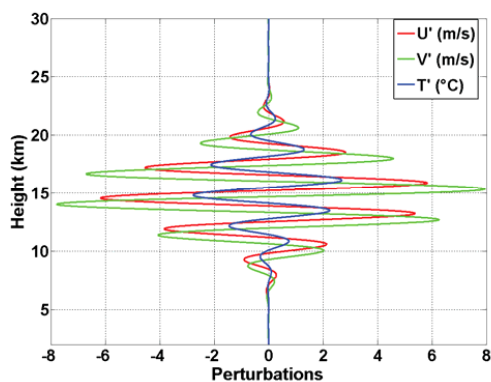


Figure 7. **(a)** Vertical profiles of temperature ($^{\circ}\text{C}$) and perturbations ($^{\circ}\text{C}$) on the left and right panels respectively from RS and RO data on 27 July at 2303, 28 July 2013 at 0200 and 1200 UTC respectively. Morlet CWT (left panel) of temperature perturbations (right panel) of RO data on 28 July 2013 at **(b)** 0200 UTC and **(c)** 1200 UTC respectively. **(d)** Cross wavelet spectrum ($\text{C}^4 \text{ km}^{-2}$) on 28 July 2013 at 0200 UTC and 1200 UTC and corresponding horizontal wavelength (km) as a function of altitudes for vertical wavelengths between 2.5 km (blue solid line) and 3 km (red solid line). Color scale: red relatively high values, blue relatively low values.

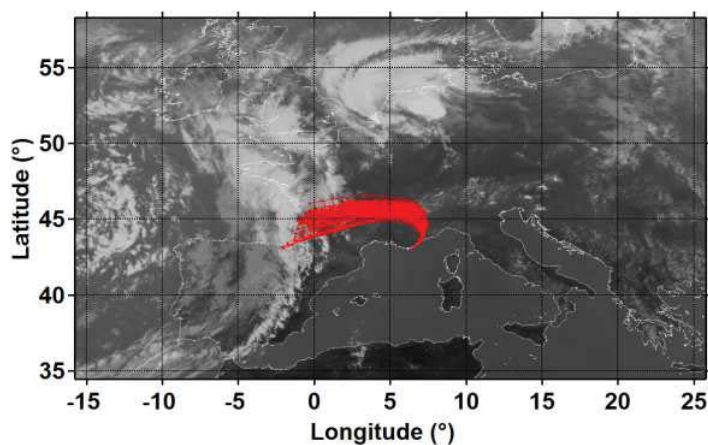


(a)

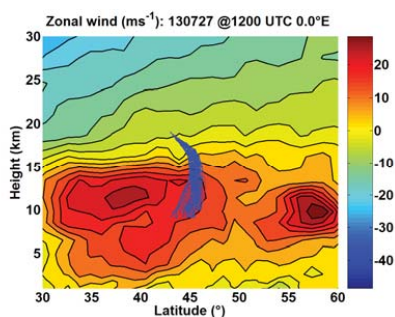


(b)

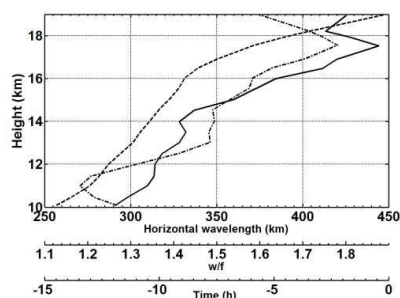
Figure 8. **(a)** Observed (blue solid line) and simulated temperature (green solid line) in units of $^{\circ}\text{C}$ (left panel) respectively on 27 July at 2303 UTC. Same as the left panel but for horizontal wind profiles (ms^{-1}). Red solid lines indicate the observed mean profile. **(b)** Simulated perturbation profiles using GW simplified linear wave polarization relations. U' , V' and T' are zonal wind (ms^{-1}), meridional wind (ms^{-1}) and temperature ($^{\circ}\text{C}$) perturbations respectively.



(a)



(b)



(c)

Figure 9. Backward rays from Ile du Levant launched at 19 km height on 28 July at 0000 UTC onto (a) georeferenced infrared GMS-3 image and (b) altitude-latitude cross section (color scale: red relatively high values, blue relatively low values) of zonal wind (ms^{-1}) at longitude of 0.0 E on 27 July at 1200 UTC. (c) Evolution of horizontal wavelength in units of km (solid line), ω/f (dash-dot line) and time in units of h (dashed line) as a function of altitude (km).

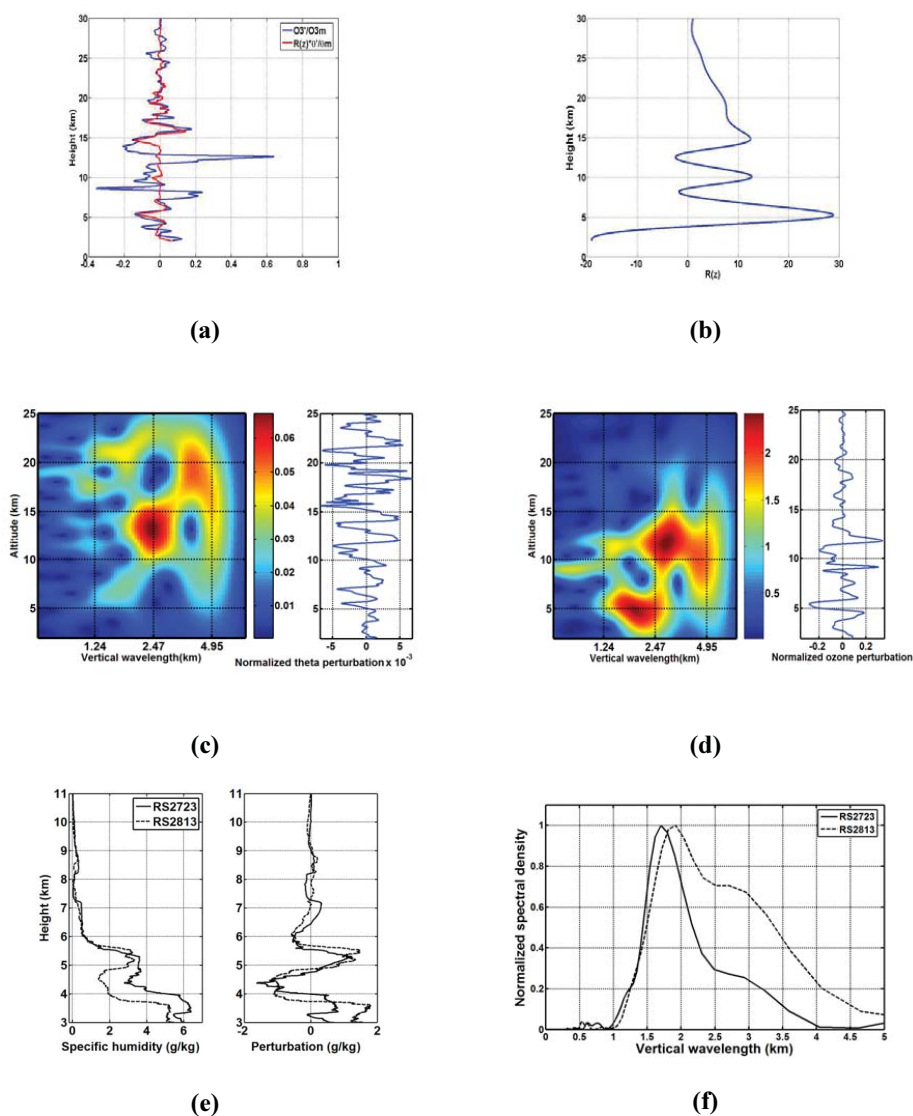


Figure 10. **(a)** Normalized perturbations of the temperature and the ozone mixing ratio for the vertical wavelength bandwidth of 1.2-4.8 km using DWT. Temperature perturbation ($^{\circ}\text{C}$) profile has been multiplied by the factor $R(z)$ **(b)** defined in section 3.6. **(c)** and **(d)** Morlet CWT (left panels) of normalized temperature and ozone concentration (ppmv) perturbations (right panels) on 28 July at 1330 UTC (color scale: red relatively high values, blue relatively low values). **(e)** Specific humidity (gkg^{-1}) and perturbations on 27 July at 2303 UTC and 28 July at 1330 UTC at heights of 3-11 km, and **(f)** corresponding normalized spectral density of specific humidity.

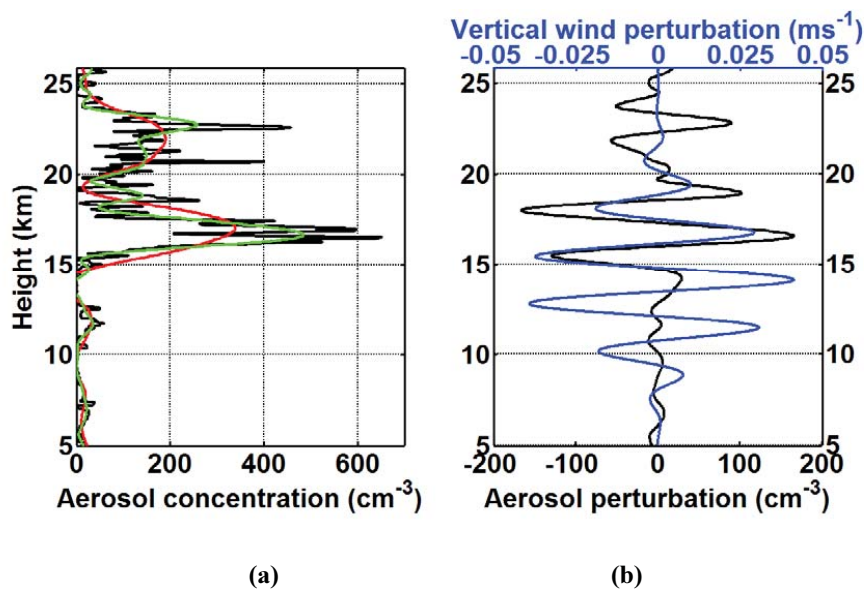


Figure 11. Vertical profiles of **(a)** aerosol concentration (cm^{-3}) and **(b)** aerosol (size class: 0.2-50 μm) perturbations with 1.6-3.2 km vertical wavelengths and simulated vertical wind perturbations (ms^{-1}) on 27 July at 2303 UTC. On left panel, black (red) solid line corresponds to raw (background) profile (cm^{-3}). The sum of the background profile and GW perturbations is drawn as green solid line.